Stabilizing the Interphase in Cobalt-free, Ultrahigh-nickel Cathodes for Lithium-ion Batteries

Michael Yi, Andrei Dolocan, and Arumugam Manthiram*

[a] Mr. M. Yi, Dr. A. Dolocan, Prof. A. Manthiram
McKetta Department of Chemical Engineering & Texas Materials Institute, The University of Texas at Austin, Austin, Texas, 78712, USA
E-mail: manth@austin.utexas.edu

Abstract: High-nickel layered oxide cathodes, such as $LiNi_{1-x-y}Mn_xCo_yO_2$ (NMC) and $LiNi_{1-x-y}Co_xAl_yO_2$ (NCA), are at the forefront for implementation in high-energy-density lithium-ion batteries. The presence of cobalt in both cathode chemistries, however, largely deters their application due to fiscal and humanitarian issues affiliated with cobalt sourcing. Increasing the Ni content drives down the Co content, but introduces additional structural and electrochemical problems attributed to high-Ni cathodes. We herein present a dually modified cobalt-free ultrahigh-nickel cathode $0.02B-LiNi_{0.99}Mg_{0.01}O_2$ (NBM) with 1 mol% Mg and 2 mol% B that exhibits a high initial 1C discharge capacity of 210 mA h g^{-1} with a 20% capacity retention improvement over 500 cycles when benchmarked against $LiNiO_2$ (LNO) in pouch full cell configurations with graphite anode. Postmortem analyses reveal the enhanced performance stems from reduced active lithium inventory loss and localized surface reactivity in the NBM cathode. The stabilized cathode-electrolyte interphase subsequently reduces transition-metal dissolution and ensuing chemical crossover to the graphite anode, which prevents further catalyzed parasitic reactions that harmfully passivate the anode surface. Altogether, this work aims to highlight the importance of electrode characterization and analysis from an interphasial viewpoint and to push the ongoing research to stabilize cobalt-free ultrahigh-Ni cathodes for industrial feasibility.

1. Introduction

The lithium-ion battery (LIB) market has seen an expeditious increase in demand for advanced energy storage systems for next-generation electric vehicles (EVs). For EVs to achieve similar cost competitiveness and performance to standard internal combustion engine vehicles (ICEVs), the US Department of Energy (DOE) estimates that LIBs will need to meet critical energy density and cost metrics of 235 W h kg^{-1} at \$100 kW h^{-1} at the pack level.[1–3] The current price of LIB packs ranges from around \$130 to 170 kW h^{-1} and it is assessed that the US can reach a cost of \$125 kW h^{-1} by 2025, which still exceeds the targeted price goal.[2,4,5] LIBs with Ni-based layered oxide cathodes have been the most prevalent battery chemistry utilized in EVs, particularly with the $LiNi_{1-x-y}Mn_xCo_yO_2$ (NMC) and $LiNi_{1-x-y}Co_xAl_yO_2$ (NCA) cathode classes.[6–8] Yet, even these chemistries now fall short of meeting the stringent DOE criteria due to inadequate energy density along with the high costs of the cathodes, primarily due to the presence of cobalt.

The price of Co has been extremely volatile in recent years and has seen a cost swing of \$46,000 ton^{-1} to > \$81,000 ton^{-1} just this past year.[9] Co is also known to be highly toxic and poses carcinogenic threats upon improper exposure.[10] Most concerningly, it is primarily sourced from the Democratic Republic of the Congo where there is major geopolitical instability and labor law ethics issues.[10–12] These concerns associated with Co sourcing have severely deterred its usage in NMC and NCA cathodes and call for alternative low-Co or Co-free compositions to be explored, such as ultrahigh-Ni cathodes (with ≥ 95 mol % Ni). Increasing the molar Ni content in these layered oxides to such levels reduces the Co content, ideally to zero, and substantially increases the specific capacity and energy density of the cathode, which helps reach the LIB metrics set by the US DOE, but also introduces large drawbacks towards battery lifetime and safety.

Challenges associated with ultrahigh-Ni cathodes, including synthesis difficulties causing a reduction of Ni^{3+} to Ni^{2+} and Li/Ni mixing,[13–15] poor electrolyte surface decomposition and

interphase formation due to highly reactive Ni^{4+} at high states of charge,[16,17] surface rock-salt phase formation and phase transformations ensuing kinetic hindrances,[18–21] transition-metal dissolution and chemical species crossover from the cathode to anode,[22–24] and particle pulverization stemming from large anisotropic lattice distortions during cycling[25–27] all drastically hindering industrial feasibility. $LiNiO_2$ (LNO), a pure Ni and ideal Co-free cathode, delivers the highest specific capacity among all Ni-based layered oxides, but consequentially suffers from the worst cycle life and safety due to these issues.

Efforts to improve the stability of high-Ni cathodes through methods, such as doping,[28,29] coating,[30,31] electrolyte engineering,[32–34] and microstructural engineering[35–37] have been in progress for many years now, but only recently has work began to shift more towards optimizing the performance of Co-free, ultrahigh-Ni cathodes like LNO. Additionally, our group has previously performed a comprehensive screening analysis of several elements that were used to treat the surface of high-Ni cathodes. By computationally and experimentally screening through several elements, it was Co that showed to be the most effective in stabilizing the cathode.[38] However, this conclusion further exemplifies why it is so difficult to move away from Co in high-Ni cathodes and indicates how hard it is to retain similar performance when it is completely removed from the cathode composition. This, therefore, necessitates further research into stabilizing Co-free, ultrahigh-Ni cathodes, such as LNO. Furthermore, postmortem analyses of the LNO cathode and the respective graphite anode after long-term cycling in a full cell configuration have not been thoroughly investigated. The dynamic electrode-electrolyte interphase evolutions from the surface to the bulk of LNO full cells, in particular, is of great interest and warrants close examination as it has been shown that such surface reactivities and resulting interphase degradations in high-Ni cathodes critically affect capacity retention.[39]

In this study, we introduce a dually modified LNO cathode $0.02B\text{-}LiNi_{0.99}Mg_{0.01}O_2$ (NBM) with 1 mol% Mg and 2 mol% B that is benchmarked against undoped LNO in both half

and full cell testing conditions, followed by advanced postmortem characterization of the cycled electrodes. The choice of Mg and B as dopants stems from the current understanding of Mg^{2+} functioning as an inert pillaring ion in the Li layer to mitigate lattice collapse due to anisotropic distortions coupled with B promoting a robust microstructure and cathode-electrolyte interphase (CEI) formation during cycling.[37,40–49] The NBM cathode exhibits a notable improvement in cycling stability with a 20% capacity retention increase over the baseline LNO cathode after long-term cycling in pouch full cells. Hybrid pulse power characterization (HPPC) tests coupled with postmortem electrochemical, X-ray diffraction (XRD), and scanning electron microscopy (SEM) analyses indicate more severe active Li loss present in the LNO cathode and less utilization in the graphite anode. As this study stems to focus on the dynamic interphasial phenomena of the electrodes, time-of-flight secondary ion mass spectrometry (TOF-SIMS) characterization is employed to assess the chemical evolutions of the electrode-electrolyte interphases after cycling. Chemical depth profiling, 3D rendering, and burst alignment imaging of key cathode and anode fragments reveal localized reactivity of the NBM cathode near the surface resulting in a thinner and more compact CEI than the LNO cathode. The stabilized CEI leads to lessened chemical crossover and catalyzed surface reactions on the graphite anode surface and results in better lithium retention over the course of cycling for the NBM cell.

2. Results and Discussion

2.1. Morphological, Elemental, and Structural Characterization

The calcined cathodes display spherical morphologies with diameters of ~ 12 μm as shown in **Figures 1a** and 1b. Figure S1 reveals SEM images of the cathode precursors prior to calcination and shows that the NBM precursor is surrounded by an amorphous coating around the entire particle. This is the coated B_2O_3 from the wet chemistry method done prior to calcination and indicates successful boron treatment onto the precursor. After calcination, the NBM cathode interestingly presents smaller and elongated primary particles compared to those of LNO and is further portrayed through the focused ion beam (FIB) cross-sectional images.

This can be explained as boron has been shown to occupy the grain boundaries near the surface in between the primary particles and alter the microstructure by suppressing grain growth during calcination.[37] XRD refinement results in Figures 1c and 1d indicate that both cathode powders have peaks native to the hexagonal α-NaFeO$_2$ structure with the *R-3m* space group with no other impurity peaks and display low degrees of Li/Ni mixing, indicating good particle crystallinity.

The elemental distribution in NBM was first analyzed with cross-sectional SEM and energy dispersive X-ray spectroscopy (EDS) mappings provided in Figure S2, which clearly reveal the presence of Ni and Mg throughout the particle. However, light elements, such as B are not easily identifiable with EDS as atoms with small atomic masses yield decreased X-ray sensitivity upon analysis. As a result, ultra-sensitive TOF-SIMS depth profiling was carried out to fully characterize the elemental distribution in the NBM cathode as shown in Figure 1e. Most of the incorporated boron indicated with the BO$^-$ fragment signal appears to largely remain near the surface indicated by the sharp peak at the start of the depth sputtering and quickly diminishes nearly to zero as more of the bulk Ni layered oxide is probed signified by the ^{62}Ni$^-$ fragment. As a sanity check, BO$^-$ depth profiling was also carried out on pristine LNO as shown in Figure S3 and it unsurprisingly shows no traceable boron detection even at the surface compared to NBM. The MgO$_2^-$ signal referring to the doped magnesium also shows a sharp peak at the start and then gradually fades but remains constant at a higher intensity signal than boron into the bulk. This is likely because Mg was added alongside Ni mixed in solution during coprecipitation to form the precursors, made possible by the similar K$_{sp}$ values of Mg(OH)$_2$ (5.61×10^{-12}) and Ni(OH)$_2$ (5.48×10^{-16}). This can yield a more uniform elemental distribution as seen with the sputtered profiles.[50] TOF-SIMS chemical mapping of the sputtering was carried out with a burst alignment mode to visualize the elemental evolution of the particles from surface to bulk shown in Figure 1f. With just 10 s of sputtering, strong BO$^-$ signals are detected on the cathode particles, corroborating the depth profile that B mainly segregates near

the surface of the NBM cathode. After extensive sputtering for one hour, nearly all BO^- signals disappear exposing the bulk NiO_2^- signal along with the less intense MgO_2^- signal. The characterizations of the cathode samples overall indicate successfully synthesized particles with good morphology and elemental distribution, which allow for appropriate comparisons of electrochemical performance and postmortem analyses to be made.

2.2. Electrochemical and Thermal Performances

2.2.1. Half-cell and full-cell cyclabilities

The electrochemical performances of the cathodes were first evaluated in Li-metal coin half cells with LP57 electrolyte which consists of 1.0 M $LiPF_6$ dissolved in ethylene carbonate (EC) and ethyl methyl carbonate (EMC) in a 3 : 7 weight ratio with 2 wt. % vinylene carbonate (VC) additive. **Figure 2a** shows the voltage curves of the cathode half cells during formation cycling. Interestingly, both LNO and NBM cathodes show essentially identical discharge capacities of ~ 242 mA h g^{-1} despite a marginally reduced Ni and Li content for NBM with both B and Mg incorporation. Upon close inspection, the voltage plateaus seen in LNO are slightly more elongated along with sharper shoulder peaks near the start and end of both charge and discharge compared to that of NBM. The dQ dV^{-1} curves in Figure 2b better depict this observation, as the peaks around 3.65 and 4.2 V for LNO are noticeably sharper and higher in intensity than those of NBM, which directly correlate to the plateaus seen in the voltage curves. These two peaks correspond to, respectively, the H1-to-M and H2-to-H3 phase transitions commonly seen in high-Ni layered oxide cathodes and indicate that LNO initially undergoes through more drastic transitions.[51] The curves also show that NBM operates at a slightly higher voltage by about 9.3 mV than LNO based on the discharge peak at around 4.16 V, suggesting that NBM yields a slightly larger energy density. Figure 2c compares the rate capabilities of LNO and NBM, which shows that the latter has a better overall capacity retention at all rates except for the fastest discharge rate of 5C, with NBM having a 77% capacity retention

compared to 79% with LNO. The slightly lower capacity retention of NBM at this rate has been noted before and is attributed to the increased Li/Ni mixing and Mg^{2+} insertion in the Li layer, which can cause some Li^+ kinetic hindrances during de-/intercalation.[45] However, this compromise for B and Mg incorporation in NBM is not very significant, as shown and should not be a demerit for assessing the feasibility of the cathode.

The half-cell cycling performances of the cathodes are shown in Figure 2d where the initial C/3 discharge capacities of both cathodes are nearly identical at ~ 229 mA h g^{-1} like that of the C/10 discharge capacities, shown in Figure 2a. NBM, however, possesses a larger capacity retention of 76% compared to that of LNO with 68% after 130 cycles. This improvement is complimented by the higher average Coulombic efficiency of NBM compared to that of LNO, as shown in Figure S4. Figure S5 additionally shows the higher degree of Li^+ reversibility in NBM as the noticeable dQ dV^{-1} phase transition peaks after 130 cycles remain more intact and present relative to the initial peaks after the 4th C/3 cycle. This can be attributed to the effects of Mg, as its presence in the Li layer has been previously shown to suppress phase transitions that result in large anisotropic lattice distortions and maintain the structural integrity and reversibility of the cathode.[45,46,49,52,53] LNO on the contrary, shows severely diminished peak intensities and shifts to higher voltages, indicating a larger kinetic hindrance buildup to Li^+ diffusion and irreversible structural degradation after many cycles.[54] This can explain the more severe voltage polarization and loss of voltage plateaus during both charge and discharge, leading to faster capacity fade seen in LNO over NBM as depicted in the voltage curve evolutions over 130 cycles in Figure S6.

Long-term cycling performances of the cathodes assembled with graphite anodes in pouch full cells are shown in Figure 2e. Both cells display a high initial 1C discharge capacity of 210 mA h g^{-1}, again showing that NBM interestingly does not suffer from an initial capacity penalty compared to LNO. After 500 deep cycles from a voltage range of 2.5 to 4.2 V, the NBM full

cell displays a better capacity retention of 65% compared to the notably worse retention of 45% for LNO. Figure 2f shows the voltage curve evolutions of C/3 cycles that were carried out every 100th cycle during long-term cycling to serve as capacity checks to better understand the capacity fading phenomena of the full cells. Initially at the 5th cycle, both cells show distinct voltage plateaus, clearly indicative of the H3-H2-H1 phase transitions that take place throughout the course of discharge. However, after the 500th cycle, all the plateaus in the LNO cell become indistinguishable from the overall curve and nearly disappear. This is evident of large structural degradation experienced by the cell as it no longer goes through such phase transitions and, therefore, does not reach the same state of charge (SOC) as it did initially, which results in its great loss of capacity upon discharge. Additionally, large vertical voltage drops are seen at the onset of discharge for LNO, to such a degree where it goes below 4.0 V at 500 cycles before delivering any capacity. This voltage slippage has been seen before with degradation in high-Ni cathodes and is attributed to severe polarization increase and impedance buildup.[55,56] Such a large polarization even at a moderately slow current rate of C/3 indicates extreme degradation of the LNO full cell. The NBM full cell, however, maintains discernable voltage plateaus even up to the 500th cycle and does not experience voltage drops to the degree at which was seen for LNO, holistically indicating better mitigated polarization and structural damage over the course of cycling. The overall voltage polarization growth throughout cycling is also mitigated for NBM over LNO as shown in Figure 2g.

2.2.2. HPPC and postmortem cell cycling

Hybrid pulse power characterization (HPPC) tests were also carried out for the pouch full cells every 100th cycle as shown in **Figure 3a**. HPPC serves as a good indicator of resembling actual driving conditions of the cells in electric vehicles by applying brief but fast discharge current pulses periodically until the lower voltage cutoff is reached. This can closely mimic the energy load profiles of actual cells as the pulses simulate abrupt acceleration and braking

8

deceleration in EVs.[57–59] Therefore, factors that contribute towards cell degradation, such as impedance and polarization growth, can be directly observed in the HPPC plots from the change in direct current internal resistances (DCIR) and SOCs of the cells upon each discharge pulse. Note that the depth of discharge (DOD) unit in the plots is defined as: 100% - SOC. Both cells also do not reach 100% DOD during the tests as the metric is referenced to the C/10 discharge capacity of the final formation cycle. The HPPC curves indicate that the DCIRs of both cells initially start with moderately high values and decrease with increasing DOD, and then abruptly increase at high DODs. This correlates well with previous results seen in the literature, which show that the Li^+ diffusion kinetics is reduced at low DODs due to the collapse in cell volume and at high DODs due to the decrease in available lithium intercalation sites.[60] Upon every 100th cycle, the maximum DOD attainable for the cells decreases due to polarization and accumulated impedance increase, which limits the overall capacity utilization. The NBM cell, however, achieves a lower resistance compared to the LNO cell at similar DODs for each HPPC test. At the 500th cycle, the NBM cell can still obtain 56% DOD with a DCIR of 132 Ω cm^2, while the LNO cell only reaches 34% DOD with a DCIR of 144 Ω cm^2. The total degree of voltage polarization and impedance is lessened for NBM compared to LNO, which allows for an extended usable capacity range.

Based on the overall electrochemical performance seen in Figures 2 and 3a, the LNO cell evidently suffers from more severe capacity decline over the NBM cell. This is additionally highlighted in the voltage curves of the reactivation cycles done on the pouch cells after 500 cycles in Figure S7, in which the LNO cell shows much more severe capacity loss and polarization compared to the NBM cell even at a slow C/10 rate. In order to identify and distinguish the cause of capacity loss for the pouch cells, the cycled cathodes were harvested and paired with fresh Li metal into coin half cells as shown in Figure 3b. After two C/10 cycles, both LNO and NBM coin cells show greatly reduced discharge capacities and large

overpotentials compared to the 3rd formation cycle discharge of their respective fresh cathode half cells, most likely from active material loss from long-term cycling.[5] The NBM cell still displays a higher capacity than the LNO cell owing to the mitigated polarization and better lithium accessibility seen with the HPPC results in Figure 3a. The key difference seen between the two cells is the notable increase in the 502nd charge capacity compared to the 501st charge capacity in the LNO cell. This indicates that some new Li is introduced into the cycled LNO cathode upon the 501st C/10 discharge from the fresh Li-metal anode, signifying that there is Li inventory loss for the LNO cathode after long-term cycling.[5,61] On the contrary, the NBM cell shows no apparent Li inventory loss, comparing the first and second C/10 cycles. In fact, the latter charge capacity is slightly less than that of the first, which suggests that some Li is getting consumed after the first cycle in order to develop a new SEI and CEI layer on the electrodes, as is typically seen with fresh coin half cells.

Likewise, coin half cells were also assembled by pairing the cycled graphite anodes of the pouch cells with fresh Li metal and were cycled twice at a C/10 rate, as seen in Figure S8. Both cells show similar decreases in discharge capacity, but lessened voltage polarization to those seen with the cathode half cells. The similar discharge capacity decays seen in the cathode and graphite half cells from their fresh counterparts suggest that the active material and Li loss experienced from the cathodes can be well correlated to the reduced Li insertion capacity of the graphite anodes. In both C/10 cycles, however, the graphite that was cycled with the NBM cathode delivers a larger discharge capacity compared to that cycled with LNO cathode, implying that there is less active Li consumption on the NBM-paired graphite. This is important as previous studies show that some of the major determinants to overall full cell capacity decrease throughout cycling is active Li and material loss in both the cathodes and graphite anodes.[57,58,61] These phenomena, in turn, will lead to worsened interfacial impedance and subsequent Li$^+$ kinetic hindrances and voltage polarization. The overall results indicate that the

LNO cathode and its respective graphite anode undergo larger degrees of degradation in all cases.

2.2.3. Thermal stability

Another important factor to consider for ultrahigh-Ni layered oxides is their thermal stability, as the highly charged cathodes can experience spinel and rock-salt phase transformations induced by Ni migration at elevated temperatures near the surfaces. Such processes are accompanied by large amounts of gas release, which can aggressively react with the surrounding electrolyte and lead to potential battery pack explosions and fires in industrial settings.[62] DSC tests were carried out to test the thermal stabilities of charged LNO and NBM cathodes around 80% state of charge as shown in Figure S9. Upon heating, LNO displays a lower exothermic peak temperature of 204 °C compared to NBM with 208 °C. The integrated heat generation of LNO of 1205 J g^{-1} also is larger than that of NBM with 1139 J g^{-1}. The improved thermal stability of NBM stems from the presence of Mg^{2+} in the Li^+ layers preventing Li/Ni mixing and B^{3+} occupying the near-surface tetrahedral sites of the lattice, which both help inhibit Ni migration-induced phase transformations and ensuing gas release during charge.[63,64]

2.3. Postmortem Structural Characterization

Bulk structural evolutions of the cathodes after cycling were characterized through XRD and SEM. After 500 cycles, both cathodes interestingly show minimal changes in the overall crystal structure compared to their pristine forms as shown in the XRD patterns in **Figures 4a and b**. The patterns from the cycled samples still retain all peaks indicative of the hexagonal α-$NaFeO_2$ structure with the *R-3m* space group. SEM images in Figures 4c and d show the cathode secondary particles after 500 cycles. Both images show noticeable particle pulverization with the LNO cathodes having a marginally higher degree of cracking. Upon closer inspection, numerous LNO cathode particles show large secondary particle cracks propagating across the

particle surfaces, while most of the NBM particles present very little to no cracks spawning on the cathodes. This helps explain the slightly larger presence of shattered particles from the LNO samples compared to the NBM samples, as continual cycling of these cracked particles can cause further mechanical pulverization from anisotropic lattice distortions typically seen with high-Ni cathodes.[48,65]

Additionally, recent studies have shown that formation of loosely packed primary particles with void and nanopore formations after calcination can contribute to microstructure degradation and hence poor cyclability.[66] This may potentially also help explain the differences in cycling between LNO and NBM as LNO was shown to be more porous with loose primary particle packing and voids compared to NBM in Figures 1a and b. However, the overall morphological differences between the two cycled cathodes through SEM do not appear too disparate even with more cracking seen on LNO. Given this understanding along with the fact that the cycling performances of the two cathodes in pouch full cells are notably different with NBM exhibiting a 20% greater capacity retention, we infer that cathode particle cracking does not appear to be the main cause of the capacity fade seen between the two samples. Rather, much of the fading may stem from the surface and ensuing interphasial instabilities of LNO over NBM, which will be further discussed in the following sections.

Rietveld refinement of the powder XRD patterns was carried out, and the obtained crystallographic parameters shown in **Table 1**. Note that for the pristine samples, NBM has slightly larger c and a lattice parameters than LNO. This unit cell expansion is likely due to the presence of Mg^{2+} in the bulk Li^+ layer and B^{3+} in the surface tetrahedral sites of the layered oxide.[45,64] The cycled cathodes show an increase in the c/a lattice parameter ratio compared to their pristine samples. Such a growth in the c/a ratio is attributed to Li deficiency in the cathodes.[61] To better predict the specific Li deficiencies, calibration curves of the c/a ratios vs. SOC for LNO and NBM were generated as shown in Figure S11 from 0% to 30% SOC. Based on the curves, the predicted Li deficiencies were extrapolated from the cycled c/a values

from Table 1, and they yield values of 12.2% and 10.0%, respectively, for LNO and NBM. The LNO and NBM cathodes have increases of, respectively, 0.38% and 0.2% in the *c/a* ratios after cycling, which indicates more intense volume variation and larger active Li loss in LNO. LNO furthermore suffers from a higher extent of Li/Ni mixing after cycling compared to NBM. Considering that boron is primarily enriched on the NBM surface as shown through TOF-SIMS sputtering results back in Figure 1, the presence of pillaring Mg^{2+} ions in the NBM bulk, occupying the Li layer prior to cycling, is believed to be mainly responsible for the reduced lattice volume change and Li/Ni mixing in NBM as indicated in previous studies.[45] The pillaring Mg^{2+} ions help lower the amount of Ni^{2+} from migrating over to the Li layer and alleviate the extent of anisotropic lattice and volume distortions during cycling, which can also help mitigate the slight particle cracking as seen with the SEM image in Figure 4d.[13,49] Additionally, the reduced volume change shown throughout cycling would expose less surface area in NBM, mitigating detrimental surface reactions with the electrolyte as opposed to LNO.

Moreover, the full-width-half-maximum (FWHM) values of the (003) and (104) diffraction peaks exhibit larger increases for LNO over NBM after cycling. Changes in the FWHM are ascribed to the varying degrees of delithiation in the cathodes. The increase in the FWHM of these peaks serves as an indicator of decreasing crystallinity in the cathode due to permanent active material loss from cation migration and irreversible Li^+ loss, which is accompanied by the eventual mechanical degradation of the cathode such as particle cracking.[5,61] However, as our cycled cathodes did not display much differences in overall cracking, we attribute the main capacity degradation mechanism at play to different surface instabilities,[67] as the varying extent of surface degradation can cause heterogeneous Li composition within the electrode and worsen the active material and Li^+ losses. This Li heterogeneity can thus explain the larger increase in the FWHM of LNO over NBM.

To better analyze the delithiation states of the cathodes, *ex-situ* charged XRD was performed, and the resulting patterns were compared to those of the pristine cathodes. Both cathodes were charged to a capacity cutoff of 240 mA h g^{-1}, which is near the end of charge (~ 87% SOC) rather than a voltage cutoff to better ensure an identical state of delithiation between the two. Figure 4e shows the XRD patterns of the pristine and charged cathodes, particularly highlighting the changes in the (003) and (110) peaks during charge. We can see that compared to the pristine states, both cathodes undergo the H2-H3 phase transition depicted by the separation of the (003) peak. Upon closer inspection, the H2-H3 phase transition is more heterogeneous and less smooth for LNO than NBM at the same SOC as indicated by the larger H2 and H3 peak separations. This, in turn, results in larger lattice volume changes for LNO during cycling as indicated by the tabulated lattice parameters detailed in Table S2. Specifically, LNO experiences more drastic anisotropic volume contractions than NBM due to the larger change in the *c* lattice parameter determined from the (003) peak. Such higher volume changes during cycling also are correlated with higher degrees of Li utilization, which results in more lattice distortion and ensuing Li loss.[27] These correlate well with our tabulated refinement data in Table 1 where we indicate a larger Li utilization loss in LNO compared to NBM over extensive cycling. Additionally, despite the larger anisotropic volume contractions for LNO, both cathodes again display similar extents of cracking degradation as previously shown by SEM images in Figures 4c and d. This indicates that these volume contractions are a contributor to, but perhaps not the main cause of capacity fade between the two cathodes, and paves well into our later discussions of how we suggest that the surface reactivities of the electrode-electrolyte interphases are the main factors of such phenomena.

2.4. Cathode-electrolyte Interphase Characterization

Understanding the formation of electrode-electrolyte interphases after cycling is the most crucial aspect of postmortem analysis as the specific surface and interphase chemistries of these

layers can heavily govern the overall cell cycling stabilities. As such, characterization of the CEIs of LNO and NBM after cycling was conducted with TOF-SIMS, which is a powerful characterization technique with ultrahigh surface sensitivity and chemical selectivity. **Figure 5a** presents normalized TOF-SIMS depth profiles of various secondary-ion fragments of interest from the cycled cathodes up a sputtering depth of nearly 180 nm. The inorganic sputtered fragments in PO_2^-/POF_2^-, LiO_2^-/LiF_2^-, and NiF_3^- represent, respectively, PF_6^- anion decomposition products from $LiPF_6$ salt, Li_2O and LiF species from electrolyte decomposition reactions, and transition-metal dissolution products. The organic fragment in C_2HO^- stems from alkyl carbonate species from carbonate solvent decomposition reactions while the $^{62}Ni^-$ fragment represents the bulk Ni layered oxide.[68,69] Both CEI depth profiles depict double-layer architectures with inorganic outer layers consisting of the phosphorus-rich fragments from $LiPF_6$ salt decomposition and hybrid inorganic-organic inner layers composed of the Li/Ni-based and organic fragments from electrolyte decomposition and transition-metal dissolution reactions. This indicates a preferential separation between the inorganic and organic species of the CEIs.

Direct depth profile comparisons of the key inorganic and organic fragments in LNO and NBM cathodes are displayed in Figure 5b, which shows that all fragments are more concentrated near the surface of NBM with higher intensity counts compared to those of LNO. Such higher surface species counts for NBM may be due to the larger surface area of NBM over LNO as confirmed by Brunauer–Emmett–Teller (BET) surface area measurements of pristine cathodes presented in Figure S12a. The larger surface area may suggest more frequent surface reactivity on NBM. However, it is the specific types of surface reactions that occur, which will influence the overall cycling performance of the cathodes more than just the larger presence of side reactions due to surface area. This can be explained by the complex reactions that the boron undergoes with the electrolyte, particularly from the $LiPF_6$ salt, and are known

to be beneficial as they help scavenge the HF present in the electrolyte and protect the CEI from electrolyte decomposition and transition-metal dissolution during cycling. TOF-SIMS 3D reconstructed depth profile images in Figure S12b clearly depict this through the localized formations of BOF^-, BOF_2^-, and $LiBO_2^-$ species near the surface of the cycled NBM cathode.[40,42]

The averaged CEI thicknesses were calculated based on the FWHMs of the normalized LiF_2^- intensities at various regions of interest and are shown in Figure 5c, indicating that NBM has a CEI thickness of ~ 72 nm and does indeed possess a thinner CEI than LNO, which has a thickness of approximately ~ 97 nm. The total integrated yields of each fragment analyzed over the entire sputtering times were calculated and are summarized in Figure 5d. Interestingly, most of the fragment counts for both LNO and NBM cathodes are similar with no drastically differing values, with the counts for PO_2^-, POF_2^-, and C_2HO^- being noticeably higher for NBM than for LNO. The fact that NBM has slightly larger fragment counts, yet possesses a thinner CEI than LNO, further indicates that the electrode-electrolyte reaction products composed of the fragments are much more localized near the surface of NBM and implies the prevention of electrolyte reactions deep into the bulk compared to that of LNO. This also highlights the fact that the larger surface area of NBM seen with the BET results does not necessarily imply worsened surface reactivity and cyclability as discussed earlier. TOF-SIMS 3D reconstructed images of the CEIs are displayed in Figure 5e and better depict the surface localization of key fragments on NBM as well as the harsh extent of the parasitic electrolyte reactions that penetrate into the depth of LNO, particularly seen with the higher concentrations of LiF_2^- and NiF_3^- fragments found deeper towards the LNO bulk. These drastic differences in the cathode surface reactivities and resulting interphase formations clearly reflect the disparities seen in the cell cyclabilities of LNO and NBM. It has also been shown that for high-Ni cathodes, such phenomena are the main culprits behind poor cathode performance compared to other general

notions, such as particle cracking.[39] Overall, the combined effects of Mg and B reducing the extent of anisotropic lattice distortions along with facilitating a robust and compact CEI bolsters the rational design of such dopants to synergistically help reduce surface and interphasial degradation.

2.5. Anode Solid-electrolyte Interphase Characterization

The reaction products that form as a result of electrolyte oxidation and transition-metal dissolution are not solely limited to the CEI. Corresponding electrolyte reduction and transition-metal induced chemical crossover reactions can harmfully passivate the SEI of the graphite anode as well as lead to active lithium loss.[70,71] Initial SEM images of the cycled graphite anodes in Figure S13 show no clear distinctions in the deposition morphologies of the anodes, but the notable differences seen in the electrochemical results in Figures 2 and 3 suggest there may be discrepancies that require higher sensitivity characterization. As such, TOF-SIMS was used to better elucidate and compare the chemical changes throughout the anode SEIs. **Figure 6a** presents the normalized depth profiles of the relevant secondary-ion fragments of interest, comprising the SEIs of the sputtered anodes. Like that of the CEI analysis, the C_2O^-/C_2HO^-, LiF_2^-/PO_2^-, and Ni^- species represent, respectively, the organic carbonate solvent reduction products, inorganic $LiPF_6$ decomposition products, and crossed over transition-metal dissolution fragments. C_5^- refers to bulk graphite while the Li^- fragment may refer to inactive lithium and/or intercalated lithium. The LNO-paired graphite profile shows a double-layer architecture with an inorganic outer layer largely consisting of the salt decomposition and chemical crossover LiF_2^-, PO_2^-, and Ni^- species and an organic inner layer comprised of C_2O^- and C_2HO^- carbonate solvent reduction fragments. Interestingly, the NBM-paired graphite profile displays a triple-layer architecture, with the outer and middle layers comprised of the same respective inorganic and organic species as seen with that of the LNO-paired graphite,

but now having its innermost layer representing the Li⁻ species, which will be further discussed later in this section.

Figure 6b illustrates the 3D rendered depth distributions of representative fragments from the profiles, which clearly shows more severe surface reactivity on the LNO-paired graphite SEI than that of the NBM-paired graphite, irrespective of the inorganic or organic nature of the species. This likely coincides with the worse CEI stability of the LNO cathode, as the transition-metal dissolution species from the CEI can migrate and deposit onto the graphite surface. This in turn, can catalyze further electrolyte reduction reactions subsequently compromising the passivity of the anode SEI as seen here.[71,72]

The SEI layer thicknesses were calculated by the FWHM of the C_2O^- species indicated by the dashed lines in Figure 6a, at multiple regions of interest with the averaged data shown in Figure 6c. The thickness of the NBM-paired graphite distinctly presents a thinner layer of around 20 nm compared to that of the LNO-paired graphite, which has a thickness of around 50 nm. Here, it is important to note that the Li⁻ species shown in the depth profiles are not used to determine the SEI layer thickness, although it clearly shows that this fragment penetrates deeper into the bulk of the NBM-paired graphite, as seen in Figure 6a. Additionally, the NBM-paired graphite has lower total integrated yields of all secondary-ion fragments stemming from electrolyte decomposition products over the LNO-paired graphite except that of Li⁻ as seen Figure 6d. The presence of Li⁻ in graphite has been attributed to "dead" lithium deposits on the SEI that are no longer capable of delivering any usable capacity and therefore leads to reduced accessible lithium inventory in the anode.[73] This is interesting, as a higher yield of Li⁻ should, therefore, indicate worsened graphite SEI formation for the NBM cell due to such dead lithium formation. However, referring to the Li | graphite half cells in Figure S8, we see that the discharge capacity is greater for the cycled NBM-paired graphite cell compared to that of the LNO cell in both the 501st and 502nd cycles, indicating a larger active lithium inventory. This

along with the fact that all other decomposition fragments in the NBM-paired graphite have lesser intensity yields, implies that the Li^- cannot entirely stem from dead lithium, but rather represents reversible intercalated lithium that still contributes to capacity.[74] Also, the fact that there is active Li loss on the cycled LNO cathode as discussed in Figure 3b, but less of a Li^- signal on the respective graphite anode, suggests that the Li^+ ions of the LNO cell are being lost in surface reactions and are not participating in de-/intercalation.

Furthermore, Figure 6e depicts chemical sputtering evolution imaging of the cycled graphite anodes from 20 s to one hour and reveals the larger presence of LiF_2^- and Ni^- species in the LNO-paired graphite even after one hour of sputtering. The NBM-paired graphite, on the contrary, was mainly saturated with the C_2^- fragment, indicating the bulk graphite is mainly detected, which suggests a thinner SEI layer formation. Such differences between the lower concentration of SEI fragments on the NBM-paired graphite over the LNO-paired graphite, yet the larger detection of Li^- within the bulk of the NBM-paired graphite, can now be explained. The electrolyte and transition-metal chemical crossover products all thinly passivate the NBM-paired graphite more so than the LNO-paired graphite, stemming from the more robustly formed NBM CEI. Due to the better passivity of the formed interphases, there is better lithium intercalation between the electrodes and hence a deeper lithiation of the graphite in the NBM cell as shown by the extended intensity of the Li^- into the graphite bulk and overall better cyclability. The deeper presence of Li^- in the depth profile also does not necessarily imply a thicker SEI layer.

3. Conclusion

The ongoing pursuit of high-energy-density cobalt-free lithium-ion batteries for EVs and other energy storage applications requires development of stabilized ultrahigh-Ni cathodes. This work herein presents a dual modification on the ideal cobalt-free cathode $LiNiO_2$ with Mg and B incorporations. Electrochemical testing of the cathodes in full cell configurations

showcases the improved performance of the NBM cathode over the LNO baseline brought by mitigated voltage polarization and capacity fade. Hybrid pulse power characterization tests during full cell cycling additionally indicate the extended depth of discharge attained for the NBM cell over the LNO cell with lessened impedance growth. Postmortem half-cell cycling and XRD analyses indicate diminished active Li loss in the NBM cathode over the course of cycling. This is brought by the Mg pillaring ions leading to alleviated anisotropic lattice volume distortions and subsequent particle cracking of the cathode. Moreover, such volume change and particle cracking exacerbate the cathode surface reactivities, which pose as the true threats to usable Li and active material loss due to the formation of inactive decomposition products from parasitic reactions between the surface and electrolyte at high states of charge. TOF-SIMS mapping characterizations reveal the B-based surface treatment placates such reactions of NBM shown through localized reaction products near the surface, resulting in a thinner and more robustly passivated CEI compared to that of the LNO cathode. The corresponding graphite anode SEI of the NBM cell as a result is better stabilized with reduced transition-metal chemical crossover and catalyzed electrolyte reduction reactions, ultimately allowing for a larger active lithium inventory retention in the NBM cell.

Overall, this work hopes to spur further developments in advancing the stabilities of cobalt-free, ultrahigh-Ni cathodes for practical energy storage applications. Future work on analyzing other promising dopants, such as Nb, W, and Al, on improving LNO stability should be considered.[75–77] In addition to cathode modifications, prospective efforts to mitigate air instability and gas release from Co-free ultrahigh-Ni cathodes will be of great importance for potential commercialization. Future work on studying performance enhancements with the cathodes and advanced electrolytes, such as novel localized-high concentration and saturated electrolytes, will also be paramount to promoting the feasibility of such battery chemistries into the global LIB market.

4. Experimental Section

Materials preparation: The cathode precursors $Ni(OH)_2$ and $Ni_{0.99}Mg_{0.01}(OH)_2$ were synthesized in-house by transition-metal hydroxide coprecipitation. 2.0 M aqueous solutions of $NiSO_4 \cdot 6H_2O$ and $MgSO_4 \cdot 7H_2O$ were prepared with their appropriate stoichiometric ratios in deionized water. Separate solutions of 4.0 M KOH and 14.8 M NH_4OH were also prepared. These solutions were all simultaneously pumped into a 10 L batch stirred tank reactor with the temperature (50 °C), pH (11.5), and stirring speed (650 rpm) all carefully controlled during the coprecipitation synthesis. The synthesized hydroxide precursors were then washed with deionized water, filtered, sieved, and dried at 100 °C overnight to remove excess water trapped in the particles. The $Ni_{0.99}Mg_{0.01}(OH)_2$ precursor was then coated with B_2O_3 via a wet chemistry method. A stoichiometric amount of B_2O_3 to yield 2 mol % B was dissolved in ethanol at 60 °C and the dried precursor was then added to the mixture, which was left to stir for around three days to ensure all the ethanol had evaporated.[40,68] To finally obtain the $LiNiO_2$ (LNO) and $0.02B\text{-}LiNi_{0.99}Mg_{0.01}O_2$ (NBM) samples, their respective metal hydroxide precursors were homogeneously mixed with $LiOH \cdot H_2O$ in molar ratios of 1 : 1.03 and calcined at, respectively, 655 °C and 670 °C for 12 h under oxygen atmosphere.

Electrochemical Testing: Cathode slurries were made by mixing the cathode powders with poly(vinylidene fluoride) (PVDF) binder and conductive carbon (Super P) in a 90 : 5 : 5 weight ratio in N-methyl-2-pyrrolidone (NMP) solvent. The slurries were cast onto Al foil with ~ 2 mA h cm^{-2} active material loadings and were calendared and dried overnight in a 120 °C vacuum oven. CR2032 coin half cells were made by pairing the cathodes punched out into 1.2 cm disks with Li-metal anodes and Celgard 2500 separator. The electrolyte used in all cells was LP57, which consists of 1.0 M $LiPF_6$ dissolved in ethylene carbonate (EC) and ethyl methyl carbonate (EMC) in a 3 : 7 weight ratio with 2 wt. % vinylene carbonate (VC) additive. For the half cells, three C/10 rate formation cycles followed by C/3 cycling between 2.8 to 4.4 V was

carried out at 25 °C (1C = 180 mA g^{-1}). For pouch full cells, graphite anodes were prepared by mixing mesocarbon microbead (MCMB) graphite powder, Super P, and PVDF binder in a 90 : 2.5 : 7.5 weight ratio with NMP into a slurry. The slurry was casted onto Cu foil with an active material loading of ~ 2.2 mA h cm^{-2} and was calendared and dried in a vacuum oven overnight at 80 °C. Pouch full cells for long-term cycling were fabricated with cathodes having an areal loading of ~ 2.0 mA h cm^{-2} and were paired with the graphite anodes for an N/P ratio of ~ 1.1. The area of the cathode (4.78 × 8.15 cm^2) was slightly smaller than that of the graphite anode (4.83 × 8.15 cm^2) to ensure complete areal coverage and utilization of the cathode. The full cells were with three C/10 formation cycles followed by C/2 charge – 1C discharge rates between 2.5 to 4.2 V for long-term cycling. A C/3 cycling step for capacity checking along with a hybrid pulse power characterization test (HPPC) were applied every 100 cycles. The HPPC testing protocol used is derived from the US Department of Energy Battery Test Manual.[59,78] All galvanostatic charge and discharge steps were followed by constant voltage steps (CV).

Materials Characterization: The cathode precursors and the calcined sample morphologies were examined with a FEI Quanta 650 field emission scanning electron microscope. Cross-sectional FIB milling for SEM and EDS of the fresh cathode samples were carried out on a Scios 2 HiVac DualBeam FIB/SEM system. Powder XRD patterns were collected with a Rigaku Miniflex 600 X-ray diffractometer with Cu K$_\alpha$ radiation (λ = 1.54184 Å) in the 2θ range of 10.0 ° – 80.0 ° with a scan step of 0.02 ° and a scan rate of 0.583 ° min^{-1}. The GSAS-II software package was used to perform Rietveld refinement of the XRD patterns.[79]

DSC testing was carried out with a NETZSCH STA 449 Jupiter thermal analysis system to analyze the thermal stabilities of the cathode samples. The cathodes were both charged to 220 mA h g^{-1} (~ 80% theorectical capacity) in Li-metal coin half cells following two C/10 formation cycles. The cathodes were then harvested from the disassembled cells in an Ar-filled glovebox and were rinsed with dimethyl carbonate (DMC). After drying, the cathodes were collected and sealed in a stainless steel crucible along with electrolyte in a ~ 3 : 2 cathode :

electrolyte weight ratio and were tightened to a torque of 0.5 N m. The thermal stability tests were conducted with a 5 °C min^{-1} heating rate from 30 °C to 350 °C under flowing Ar gas.

The electrode-electrolyte interphase characterization was carried out with TOF-SIMS with a TOF.SIMS 5 spectrometer (ION-TOF GmbH). The analysis chamber was maintained at an ultra-high vacuum state of 2×10^{-9} mbar. All detected secondary ions of interest had a mass resolution of > 5,000. A 30 keV Bi$^+$ ion analysis beam was used for both depth profiling and high lateral resolution mapping with, respectively, high current mode and burst alignment mode. Depending on the secondary ion polarity, a 500 eV Cs$^+$ (negative) or a 1 keV O^{2+} (positive) ion beam was used to sputter the cycled electrodes. The typical sputtering and analysis areas were, respectively, 300×300 μm^2 and 100×100 μm^2. The electrode samples were rinsed with DMC, dried in the glovebox antechamber, and then were prepared onto the sample holder. The samples were transferred to the analysis instrument via an air-free capsule.

Supporting Information

Supporting Information is available from the Wiley Online Library or from the author.

Conflict of Interest

The corresponding author (A. M.) is a co-founder of TexPower EV Technologies Inc., a start-up company focusing on cobalt-free cathode materials for lithium-based batteries.

Received: ((will be filled in by the editorial staff))
Revised: ((will be filled in by the editorial staff))
Published online: ((will be filled in by the editorial staff))

References

[1] W. Li, E. M. Erickson, A. Manthiram, *Nat. Energy* **2020**, *5*, 26.

[2] R. Schmuch, R. Wagner, G. Hörpel, T. Placke, M. Winter, *Nat. Energy* **2018**, *3*, 267.

[3] U.S. DRIVE Electrochemical Energy Storage Technical Team Roadmap. https://www.osti.gov/biblio/1220126 (accessed Nov 2022).

[4] Cutting cobalt, *Nat. Energy* **2020**, *5*, 825.

[5] S. Lee, W. Li, A. Dolocan, H. Celio, H. Park, J. H. Warner, A. Manthiram, *Adv. Energy Mater.* **2021**, 2100858.

[6] L. Mu, Z. Yang, L. Tao, C. K. Waters, Z. Xu, L. Li, S. Sainio, Y. Du, H. L. Xin, D. Nordlund, F. Lin, *J. Mater. Chem. A* **2020**, *8*, 17487.

[7] X. Wang, Y. Ding, Y. Deng, Z. Chen, *Adv. Energy Mater.* **2020**, *10*, 1903864.

[8] M. Li, J. Lu, *Science* **2020**, *367*, 979.

[9] LME Cobalt | London Metal Exchange (accessed Nov 2022).

[10] C. B. L. Nkulu, L. Casas, V. Haufroid, T. D. Putter, N. D. Saenen, T. Kayembe-Kitenge, P. M. Obadia, D. K. W. Mukoma, J.-M. L. Ilunga, T. S. Nawrot, O. L. Numbi, E. Smolders, B. Nemery, *Nat. Sustain.* **2018**, *1*, 495.

[11] S. S. Sharma, A. Manthiram, *Energ. Environ. Sci.* **2020**, *13*, 4087.

[12] E. A. Olivetti, G. Ceder, G. G. Gaustad, X. Fu, *Joule* **2017**, *1*, 229.

[13] W. Liu, P. Oh, X. Liu, M. Lee, W. Cho, S. Chae, Y. Kim, J. Cho, *Angewandte Chemie Int. Ed.* **2015**, *54*, 4440.

[14] X. Li, A. Gao, Z. Tang, F. Meng, T. Shang, S. Guo, J. Ding, Y. Luo, D. Xiao, X. Wang, D. Su, Q. Zhang, L. Gu, *Adv. Funct. Mater.* **2021**, 2010291.

[15] M. Bianchini, M. Roca-Ayats, P. Hartmann, T. Brezesinski, J. Janek, *Angewandte Chemie Int. Ed.* **2019**, *58*, 10434.

[16] J. Li, L. E. Downie, L. Ma, W. Qiu, J. R. Dahn, *J. Electrochem. Soc.* **2015**, *162*, A1401.

[17] L. E. Downie, S. R. Hyatt, J. R. Dahn, *J. Electrochem. Soc.* **2016**, *163*, A35.

[18] Y.-S. Kang, S. Y. Park, K. Ito, Y. Kubo, Y. Shin, D. Y. Kim, D.-H. Seo, S. Kim, J.-H. Park, S.-G. Doo, M. Koh, J. A. Seo, K. Park, *J. Power Sources* **2021**, *490*, 229542.

[19] F. Lin, I. M. Markus, D. Nordlund, T.-C. Weng, M. D. Asta, H. L. Xin, M. M. Doeff, *Nat. Commun.* **2014**, *5*, 3529.

[20] B. Strehle, F. Friedrich, H. A. Gasteiger, *J. Electrochem. Soc.* **2021**, *168*, 050512.

[21] F. Friedrich, B. Strehle, A. T. S. Freiberg, K. Kleiner, S. J. Day, C. Erk, M. Piana, H. A. Gasteiger, *J. Electrochem. Soc.* **2019**, *166*, A3760.

[22] J. A. Gilbert, I. A. Shkrob, D. P. Abraham, *J. Electrochem. Soc.* **2017**, *164*, A389.

[23] S. J. Wachs, C. Behling, J. Ranninger, J. Möller, K. J. J. Mayrhofer, B. B. Berkes, *ACS Appl. Mater. Inter.* **2021**.

[24] H. Y. Asl, A. Manthiram, *J. Am. Chem. Soc.* **2020**, *142*, 21122.

[25] H. Li, A. Liu, N. Zhang, Y. Wang, S. Yin, H. Wu, J. R. Dahn, *Chem. Mater.* **2019**, *31*, 7574.

[26] P. Yan, J. Zheng, J. Liu, B. Wang, X. Cheng, Y. Zhang, X. Sun, C. Wang, J.-G. Zhang, *Nat. Energy.* **2018**, *3*, 600.

[27] W. Li, H. Y. Asl, Q. Xie, A. Manthiram, *J. Am. Chem. Soc.* **2019**, *141*, 5097.

[28] H. Yang, H. Wu, M. Ge, L. Li, Y. Yuan, Q. Yao, J. Chen, L. Xia, J. Zheng, Z. Chen, J. Duan, K. Kisslinger, X. C. Zeng, W. Lee, Q. Zhang, J. Lu, *Adv. Funct. Mater.* **2019**, *29*, 1808825.

[29] P. Oh, J. Yun, S. Park, G. Nam, M. Liu, J. Cho, *Adv. Energy. Mater.* **2020**, 2003197.

[30] X. Wang, Q. Wu, S. Li, Z. Tong, D. Wang, H. L. Zhuang, X. Wang, Y. Lu, *Energy Storage Mater.* **2021**, *37*, 67.

[31] M. Yoon, Y. Dong, J. Hwang, J. Sung, H. Cha, K. Ahn, Y. Huang, S. J. Kang, J. Li, J. Cho, *Nat. Energy* **2021**, *6*, 362.

[32] Y. Chen, W. Zhao, Q. Zhang, G. Yang, J. Zheng, W. Tang, Q. Xu, C. Lai, J. Yang, C. Peng, *Adv. Funct. Mater.* **2020**, *30*, 2000396.

[33] S. Tan, W. Wang, Y. Tian, S. Xin, Y. Guo, *Adv. Funct. Mater.* **2021**, 2105253.

[34] X. Cao, H. Jia, W. Xu, J.-G. Zhang, *J. Electrochem. Soc.* **2021**, *168*, 010522.

[35] Y. Su, G. Chen, L. Chen, W. Li, Q. Zhang, Z. Yang, Y. Lu, L. Bao, J. Tan, R. Chen, S. Chen, F. Wu, *ACS Appl. Mater. Inter.* **2018**, *10*, 6407.

[36] X. Xu, H. Huo, J. Jian, L. Wang, H. Zhu, S. Xu, X. He, G. Yin, C. Du, X. Sun, *Adv. Energy Mater.* **2019**, *9*, 1803963.

[37] C. Jung, D. Kim, D. Eum, K. Kim, J. Choi, J. Lee, H. Kim, K. Kang, S. Hong, *Adv. Funct. Mater.* **2021**, 2010095.

[38] Y. Kim, H. Park, K. Shin, G. Henkelman, J. H. Warner, A. Manthiram, *Adv. Energy Mater.* **2021**, *11*, 2101112.

[39] Q. Xie, Z. Cui, A. Manthiram, *Adv. Mater.* **2021**, 2100804.

[40] Q. Xie, W. Li, A. Dolocan, A. Manthiram, *Chem. Mater.* **2019**, *31*, 8886.

[41] Y.-J. Guo, C.-H. Zhang, S. Xin, J.-L. Shi, W.-P. Wang, M. Fan, Y.-X. Chang, W.-H. He, E. Wang, Y.-G. Zou, X. Yang, F. Meng, Y.-Y. Zhang, Z.-Q. Lei, Y.-X. Yin, Y.-G. Guo, *Angewandte Chemie Int. Ed.* **2022**.

[42] W. Wang, L. Wu, Z. Li, K. Huang, Z. Chen, C. Lv, H. Dou, X. Zhang, *Chemelectrochem* **2021**.

[43] S. F. Amalraj, R. Raman, A. Chakraborty, N. Leifer, R. Nanda, S. Kunnikuruvan, T. Kravchuk, J. Grinblat, V. Ezersky, R. Sun, F. L. Deepak, C. Erk, X. Wu, S. Maiti, H. Sclar, G. Goobes, D. T. Major, M. Talianker, B. Markovsky, D. Aurbach, *Energy Storage Mater.* **2021**, *42*, 594.

[44] S.-H. Han, J. H. Song, T. Yim, Y.-J. Kim, J.-S. Yu, S. Yoon, *J. Electrochem. Soc.* **2016**, *163*, A748.

[45] Q. Xie, W. Li, A. Manthiram, *Chem. Mater.* **2019**, *31*, 938.

[46] W. M. Seong, A. Manthiram, *ACS Appl. Mater. Inter.* **2020**, *12*, 43653.

[47] H. Li, M. Cormier, N. Zhang, J. Inglis, J. Li, J. R. Dahn, *J. Electrochem. Soc.* **2019**, *166*, A429.

[48] A. Gomez-Martin, F. Reissig, L. Frankenstein, M. Heidbüchel, M. Winter, T. Placke, R. Schmuch, *Adv. Energy Mater.* **2022**, 2103045.

[49] C. Pouillerie, L. Croguennec, P. Biensan, P. Willmann, C. Delmas, *J. Electrochem. Soc.* **2000**, *147*, 2061.

[50] D. R. Lide, CRC Press/Taylor and Francis Group, Boca Raton, FL, **2007**, pp. 118–119.

[51] H. Li, N. Zhang, J. Li, J. R. Dahn, *J. Electrochem. Soc.* **2018**, *165*, A2985.

[52] A. Liu, N. Zhang, H. Li, J. Inglis, Y. Wang, S. Yin, H. Wu, J. R. Dahn, *J. Electrochem. Soc.* **2039**, *166*, A4025.

[53] T. Sattar, S.-J. Sim, S.-H. Lee, B.-S. Jin, H.-S. Kim, *Solid State Ionics* **2022**, *378*, 115886.

[54] J. Li, J. Harlow, N. Stakheiko, N. Zhang, J. Paulsen, J. Dahn, *J. Electrochem. Soc.* **2018**, *165*, A2682.

[55] M. Yi, W. Li, A. Manthiram, *Chem. Mater.* **2022**, *34*, 629.

[56] W. Li, S. Lee, A. Manthiram, *Adv. Mater.* **2020**, *32*, 2002718.

[57] J. A. Gilbert, J. Bareño, T. Spila, S. E. Trask, D. J. Miller, B. J. Polzin, A. N. Jansen, D. P. Abraham, *J. Electrochem. Soc.* **2016**, *164*, A6054.

[58] D. P. Abraham, D. W. Dees, J. Christophersen, C. Ho, A. N. Jansen, *Int. J. Energ. Res.* **2010**, *34*, 190.

[59] J. P. Christophersen, U.S. Department of Energy Vehicle Technologies Program: Battery Test Manual for Plug-In Hybrid Electric Vehicles; Idaho National Lab, **2014**.

[60] C. Hong, Q. Leng, J. Zhu, S. Zheng, H. He, Y. Li, R. Liu, J. Wan, Y. Yang, *J. Mater. Chem. A* **2020**, *8*, 8540.

[61] W. Li, X. Liu, H. Celio, P. Smith, A. Dolocan, M. Chi, A. Manthiram, *Adv. Energy Mater.* **2018**, *8*, 1703154.

[62] Y. Wu, X. Liu, L. Wang, X. Feng, D. Ren, Y. Li, X. Rui, Y. Wang, X. Han, G.-L. Xu, H. Wang, L. Lu, X. He, K. Amine, M. Ouyang, *Energy Storage Mater.* **2021**, *37*, 77.

[63] K. Min, S.-W. Seo, Y. Y. Song, H. S. Lee, E. Cho, *Phys. Chem. Chem. Phys.* **2016**, *19*, 1762.

[64] L. Pan, Y. Xia, B. Qiu, H. Zhao, H. Guo, K. Jia, Q. Gu, Z. Liu, *J. Power Sources* **2016**, *327*, 273.

[65] H. Yu, Y. Cao, L. Chen, Y. Hu, X. Duan, S. Dai, C. Li, H. Jiang, *Nat. Commun.* **2021**, *12*, 4564.

[66] H. Park, H. Park, K. Song, S. H. Song, S. Kang, K.-H. Ko, D. Eum, Y. Jeon, J. Kim, W. M. Seong, H. Kim, J. Park, K. Kang, *Nat. Chem.* **2022**, *14*, 614.

[67] R. Pan, E. Jo, Z. Cui, A. Manthiram, *Adv. Funct. Mater.* **2022**, 2211461.

[68] Z. Cui, Q. Xie, A. Manthiram, *Adv. Energy Mater.* **2021**, 2102421.

[69] J. Li, W. Li, Y. You, A. Manthiram, *Adv. Energy Mater.* **2018**, *8*, 1801957.

[70] P. Verma, P. Maire, P. Novák, *Electrochim. Acta* **2010**, *55*, 6332.

[71] D. R. Vissers, Z. Chen, Y. Shao, M. Engelhard, U. Das, P. Redfern, L. A. Curtiss, B. Pan, J. Liu, K. Amine, *ACS Appl. Mater. Inter.* **2016**, *8*, 14244.

[72] W. Li, X. Liu, Q. Xie, Y. You, M. Chi, A. Manthiram, *Chem. Mater.* **2020**, *32*, 7796.

[73] K. Dong, Y. Xu, J. Tan, M. Osenberg, F. Sun, Z. Kochovski, D. T. Pham, S. Mei, A. Hilger, E. Ryan, Y. Lu, J. Banhart, I. Manke, *ACS Energy Lett.* **2021**, 1719.

[74] Y. Yamagishi, H. Morita, Y. Nomura, E. Igaki, *J. Phys. Chem. Lett.* **2021**, *12*, 4623.

[75] C. Geng, D. Rathore, D. Heino, N. Zhang, I. Hamam, N. Zaker, G. A. Botton, R. Omessi, N. Phattharasupakun, T. Bond, C. Yang, J. R. Dahn, *Adv. Energy Mater.* **2021**, 2103067.

[76] X. Kong, D. Li, E. O. Fedorovskaya, T. Kallio, X. Ren, *Int. J. Energy Res.* **2021**, *45*, 10489.

[77] Q. Hao, F. Du, T. Xu, Q. Zhou, H. Cao, Z. Fan, C. Mei, J. Zheng, *J. Electroanal. Chem.* **2022**, *907*, 116034.

[78] R. Sim, S. Lee, W. Li, A. Manthiram, *ACS Appl. Mater. Inter.* **2021**, *13*, 42898.

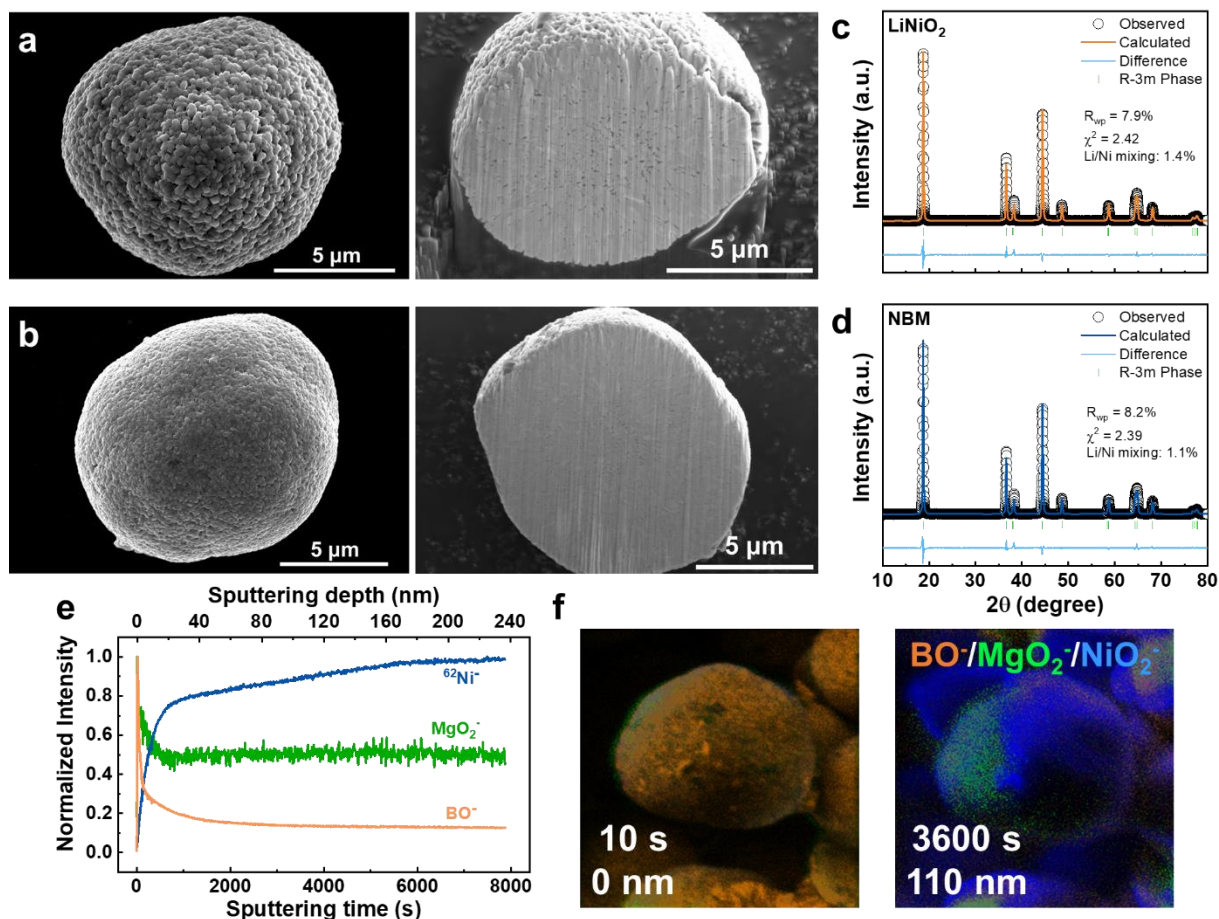[79] B. H. Toby, R. B. V. Dreele, *J. Appl. Crystallogr.* **2013**, *46*, 544.

Figure 1. Morphological, elemental, and structural characterizations of LNO and NBM cathode particles. SEM images of secondary particles and respective FIB cross sections of (a) LNO and (b) NBM. Rietveld refinement results of the XRD patterns of pristine (c) LNO and (d) NBM cathode powders. (e) TOF-SIMS depth profiles of $^{62}Ni^-$, MgO_2^-, and BO^- fragments in pristine NBM. (f) TOF-SIMS chemical mapping carried out in the burst alignment mode of pristine NBM particles, depicting BO^-, MgO_2^-, and NiO_2^- fragments after Cs^+ sputtering from 10 s up to 1 h.
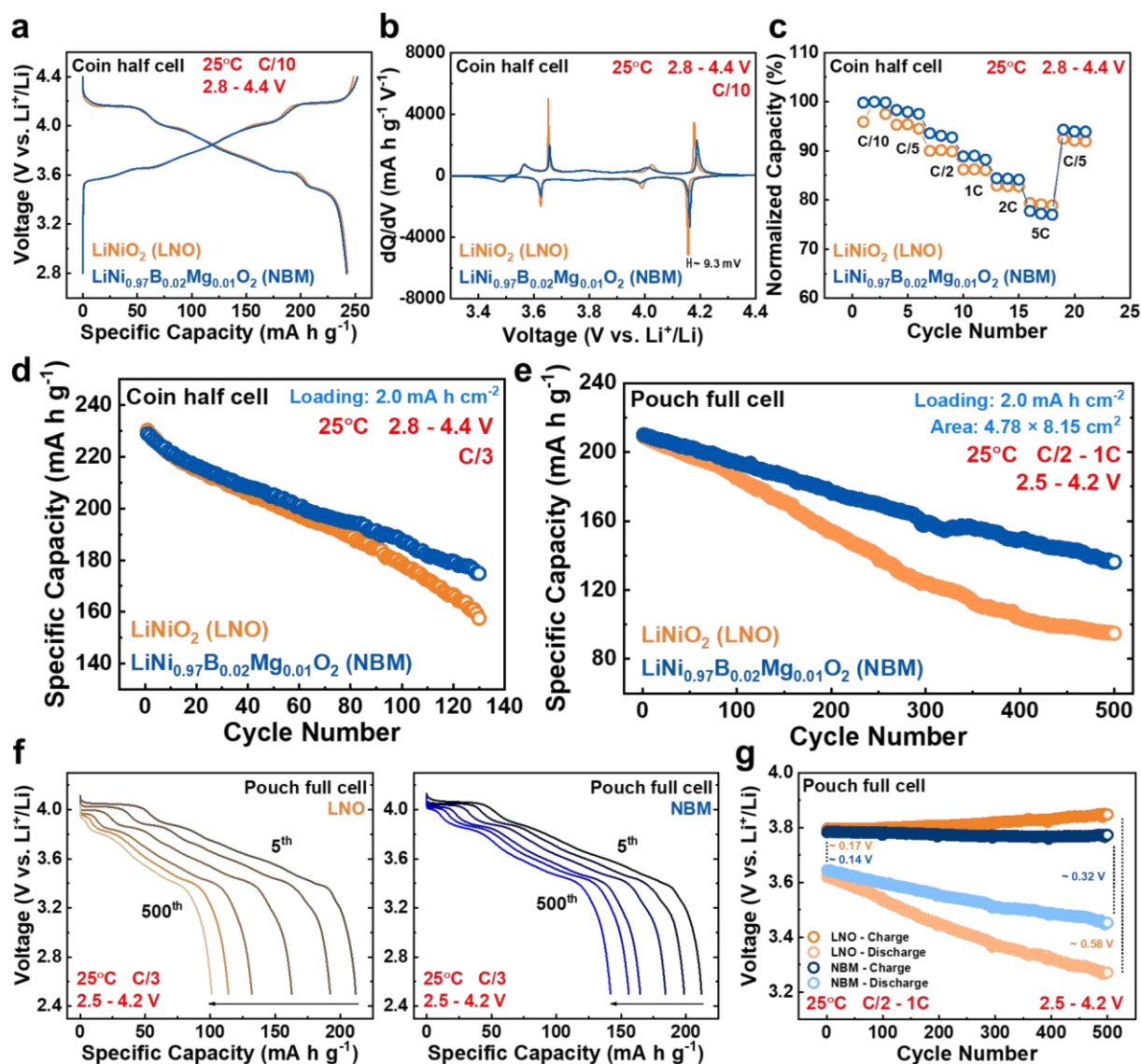
Figure 2. Electrochemical performance of LNO and NBM cathodes paired with Li-metal anodes in coin half cells and graphite anodes in pouch full cells. (a) Charge and discharge voltage profiles along with (b) dQ dV^{-1} curves of both cathodes at the third C/10 formation cycle. (c) Normalized rate capability tests and (d) half-cell cycling of cathodes. (e) Pouch full cell cycling performance and (f) C/3 discharge voltage curve evolutions every 100 cycles. (g) Average charge and discharge voltage changes over long-term full cell cycling. See Table S1 for the performance metrics of other related LNO work.
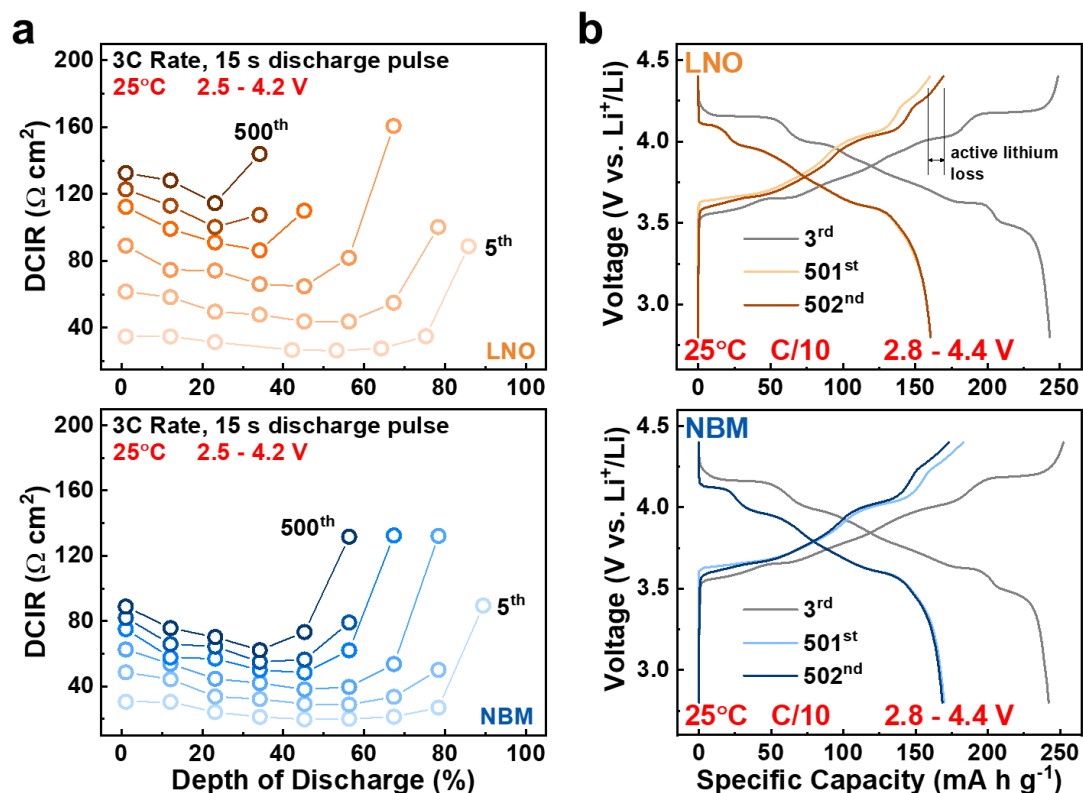
Figure 3. (a) HPPC results of LNO and NBM cathodes paired with graphite anodes in pouch full cells that were carried out every 100th cycle. The direct current internal resistances were calculated only for successful pulses that have gone through the entire duration of the discharge pulse period. (b) Voltage curves of cycled cathodes harvested from pouch full cells paired with fresh Li metal in half cells.
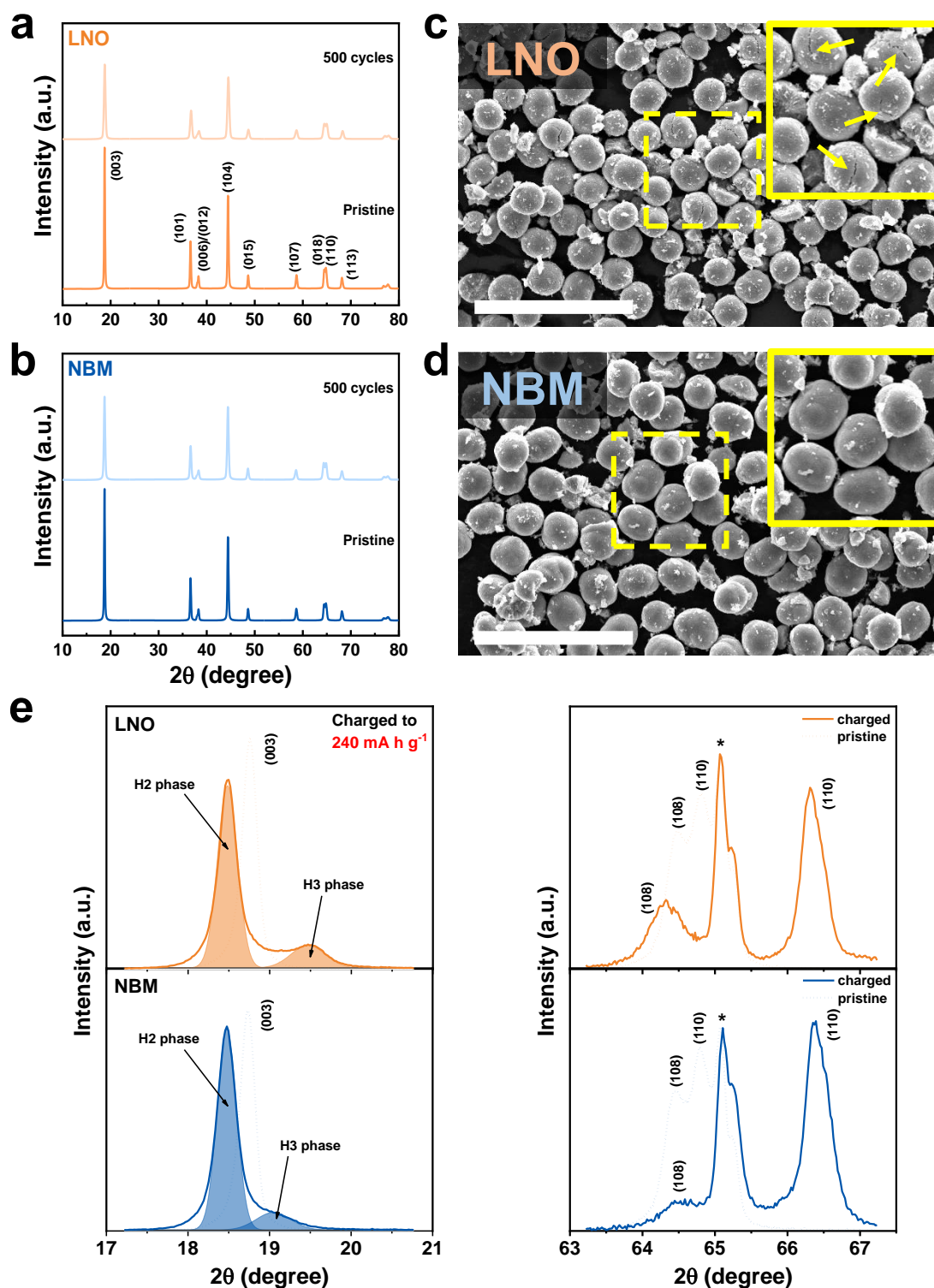
31

Figure 4. Powder XRD patterns of (a) LNO and (b) NBM cathodes before and after 500 cycles in pouch full cells. Rietveld refinement results are shown in Figure S10. SEM images of the cycled (c) LNO and (d) NBM cathodes. (e) XRD patterns of pristine and charged electrodes. The peak with the asterisk refers to contributions from PVDF, carbon, and the Al current collector of the cathodes. See Table S2 for the lattice parameters obtained from the XRD patterns in (e). The scale bars in both images are 50 μm.

Table 1. Crystallographic parameters of pristine and cycled LNO and NBM cathodes obtained with Rietveld refinement of the XRD patterns. See Tables S3-6 for the atomic sites, fractions, and tabulated refinement data for the pristine and cycled cathodes.

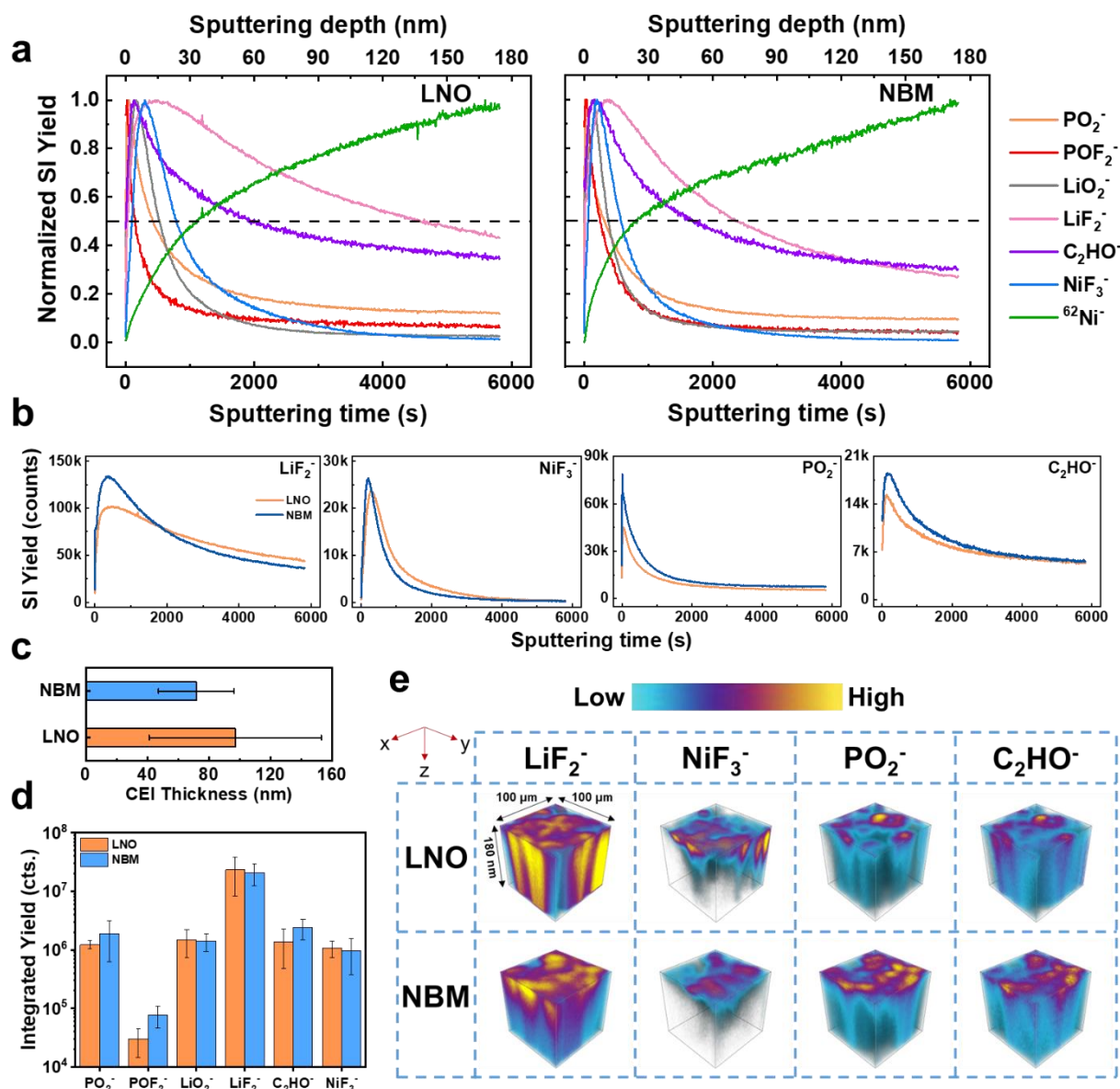| Sample	c [Å]	a [Å]	c/a	Li^+/Ni^{2+} mixing [%]	FWHM (003) [°]	FWHM (104) [°]
Pristine LNO	14.1898	2.8745	4.9360	1.4	0.18	0.28
Cycled LNO	14.2184	2.8697	4.9547	2.7	0.36	0.46
Pristine NBM	14.2058	2.8749	4.9413	1.1	0.18	0.26
Cycled NBM	14.2306	2.8743	4.9510	2.4	0.30	0.36

Figure 5. (a) Normalized TOF-SIMS depth profiles of surface and bulk fragments composing the cathode-electrolyte interphase of LNO and NBM cathodes after 500 cycles in pouch full cells. (b) TOF-SIMS intensity depth profile comparison of representative inorganic and organic secondary-ion fragments present in the CEI of the cycled LNO and NBM cathodes. Calculated average (c) CEI thicknesses and (d) integrated yields of the secondary-ion fragments. (e) 3D rendering visualization of the selected secondary-ion fragments in (b) showing the change in concentration from the surface to bulk of the cycled cathodes. See Table S7 for tabulated integrated intensity data.
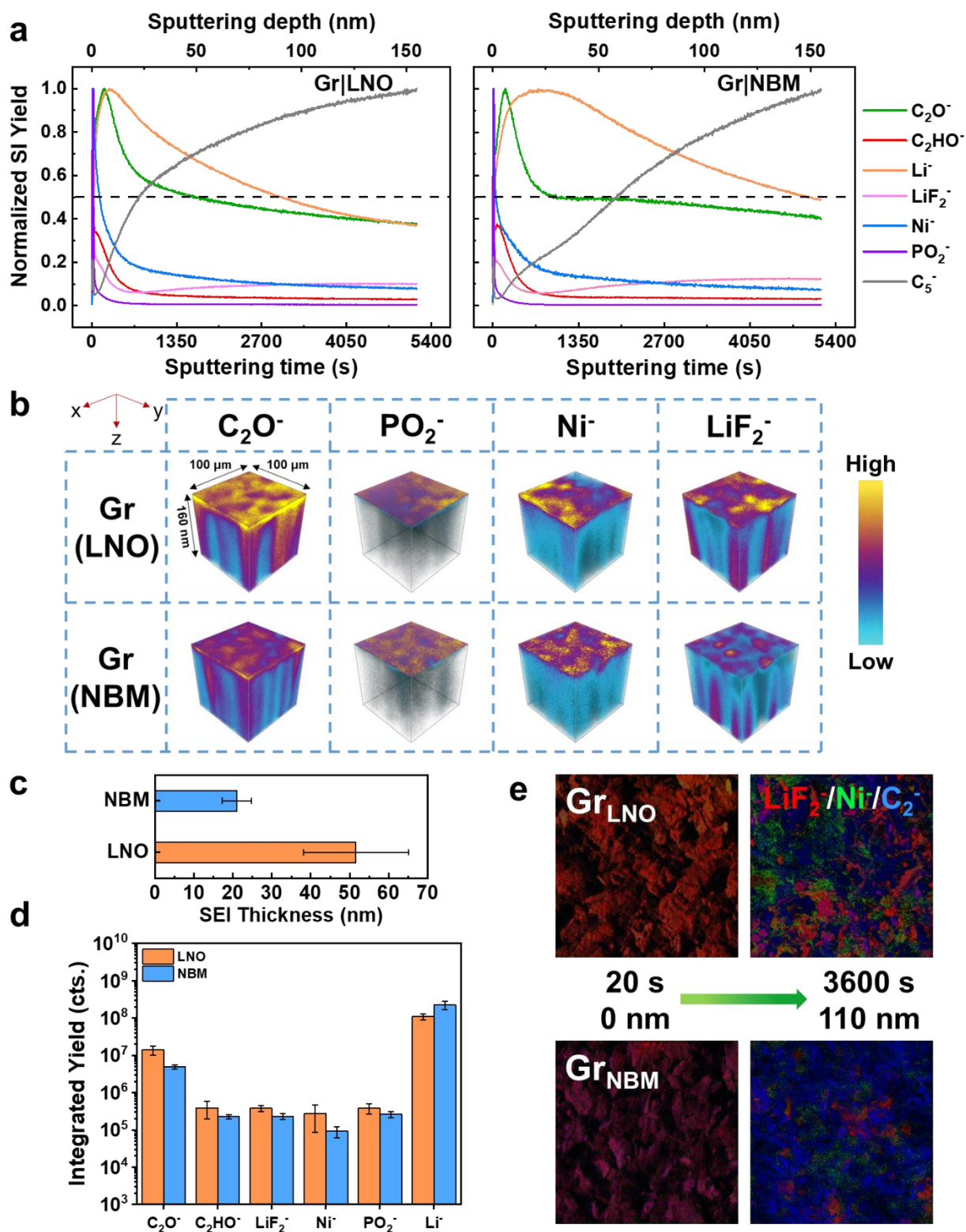
Figure 6. (a) Normalized TOF-SIMS depth profiles of surface and bulk fragments composing the solid-electrolyte interphase of graphite anodes paired with the corresponding LNO and NBM cathodes after 500 cycles in pouch full cells. (b) 3D rendering visualization of selected secondary-ion fragments of the cycled graphite anodes. Calculated average (c) SEI thicknesses and (d) integrated yields of the secondary-ion fragments. (e) TOF-SIMS chemical mapping evolutions done in burst alignment mode of key fragments composing the graphite SEI after Cs^+ sputtering from 20 s up to 1 h. See Table S8 for tabulated integrated intensity data.

Table of Contents Entry

The incorporation of Mg and B in cobalt-free LiNiO$_2$ cathodes boosts the structural integrity of the cathode, resulting in larger active lithium utilization along with a robustly passivated cathode-electrolyte interface. This in turn allows for reduced transition-metal dissolution and chemical crossover, inhibiting catalyzed reactions that can detrimentally passivate the graphite anode and holistically leading to better cyclability.

Michael Yi, Andrei Dolocan, and Arumugam Manthiram*

Stabilizing the Interphase in Cobalt-free, Ultrahigh-nickel Cathodes for Lithium-ion Batteries

Supporting Information

Stabilizing the Interphase in Cobalt-free, Ultrahigh-nickel Cathodes for Lithium-ion Batteries

Michael Yi, Andrei Dolocan, and Arumugam Manthiram[*]

Mr. M. Yi, Dr. A. Dolocan, Prof. A. Manthiram
McKetta Department of Chemical Engineering & Texas Materials Institute, The University of Texas at Austin, Austin, Texas, 78712, USA

*Corresponding author. Tel: +1-512-471-1791; fax: +1-512-471-7681.
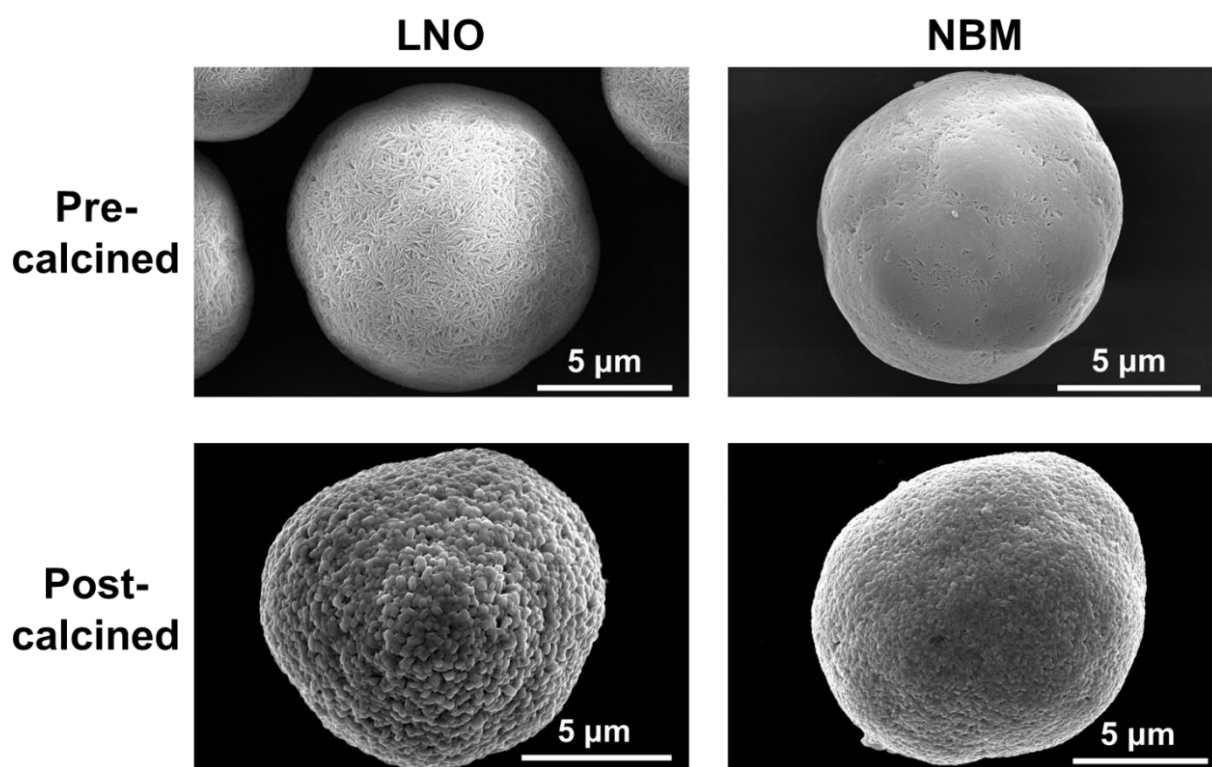E-mail address: manth@austin.utexas.edu (A. Manthiram)

Figure S1. SEM images of LNO and NBM cathode particles before and after calcination.
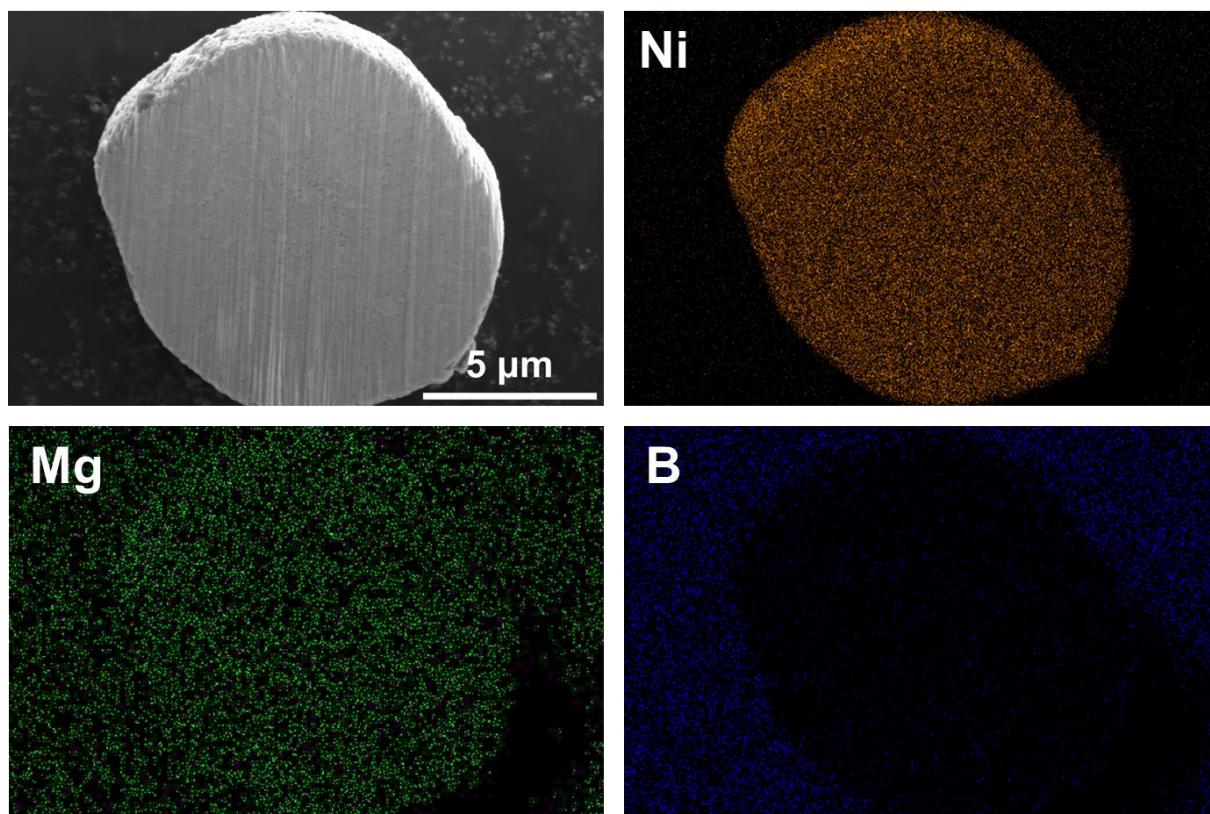
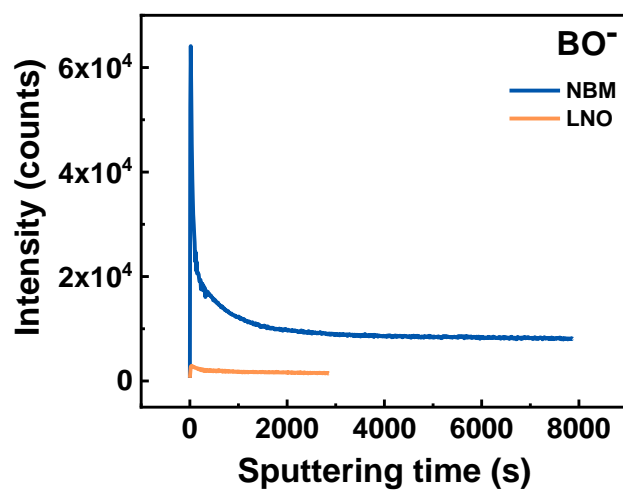**Figure S2.** FIB cross-sectional SEM images and EDS mapping of a pristine NBM cathode particle.

Figure S3. TOF-SIMS depth profile comparison of the BO⁻ fragment for pristine LNO and NBM cathodes.
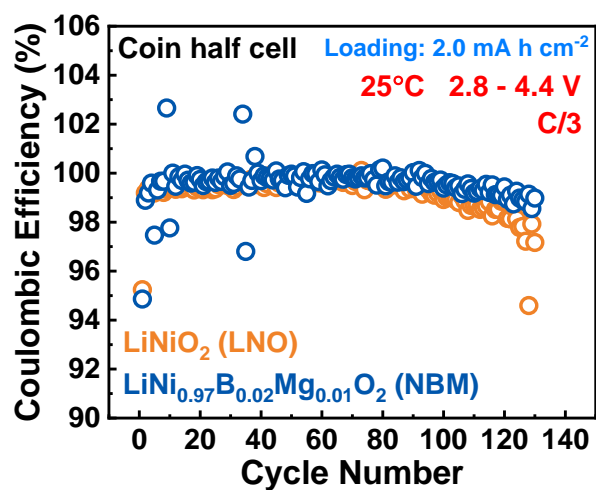
Figure S4. Coulombic efficiencies of LNO and NBM cathodes in Li-metal coin half cells over the course of 130 cycles.
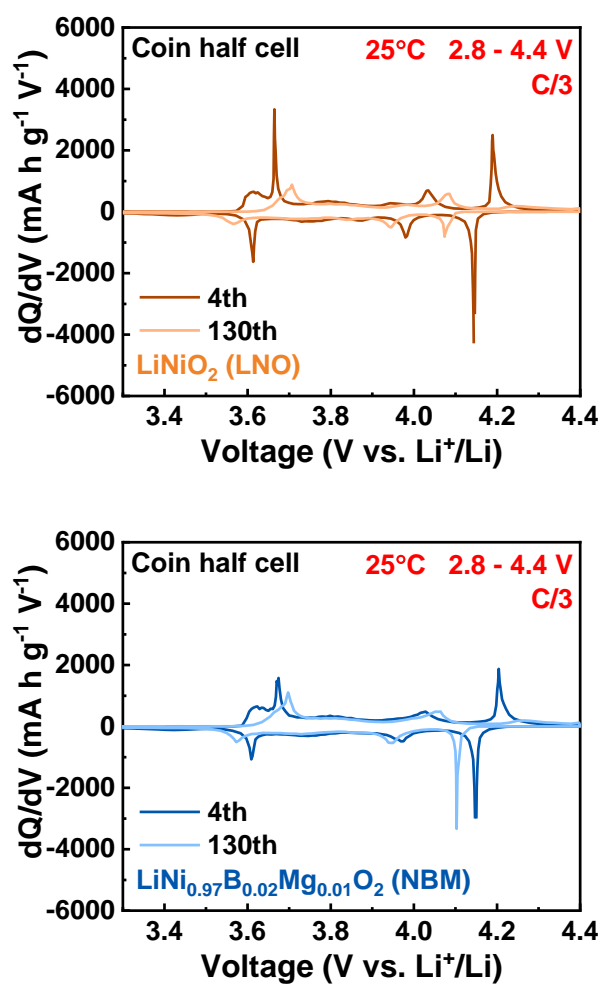
Figure S5. dQ dV^{-1} curves of LNO and NBM cathodes in Li-metal coin half cells at the 130th cycle.
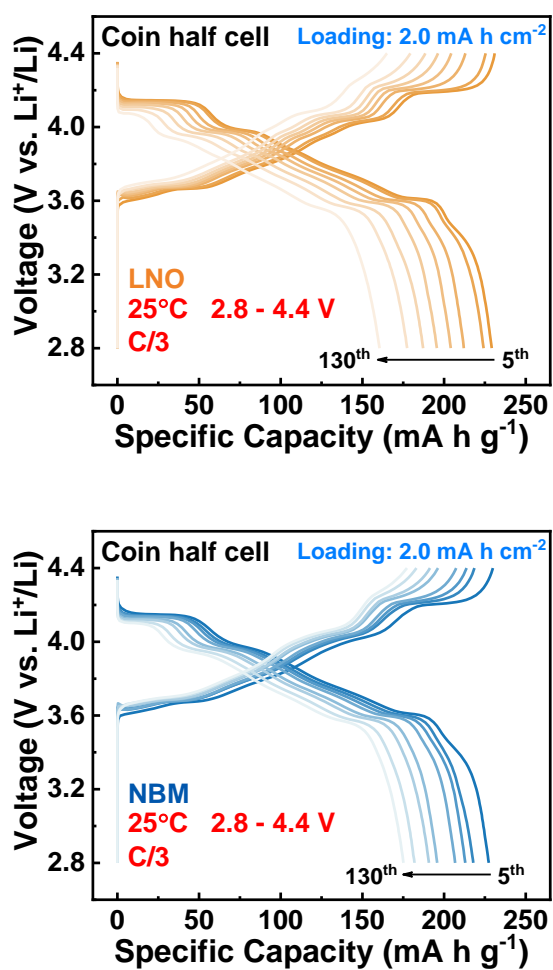
Figure S6. Charge and discharge voltage curve evolutions of LNO and NBM cathodes in Li-metal half cells over 5 to 130 cycles.
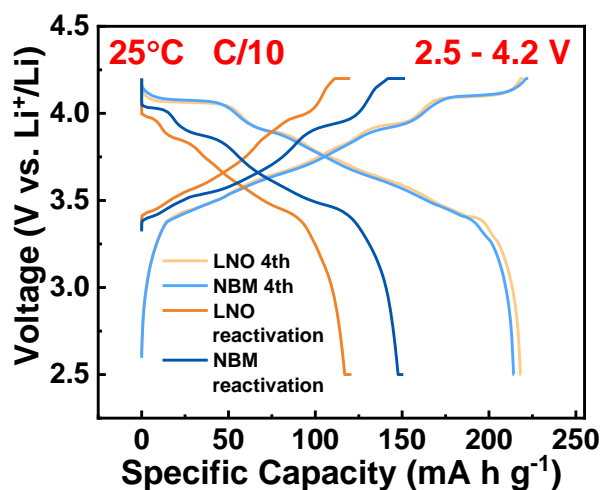
Figure S7. Charge and discharge voltage curves of a single reactivation cycle carried out at a C/10 rate in LNO and NBM pouch full cells after 500 cycles compared to the curves of the 4th C/10 formation cycle.
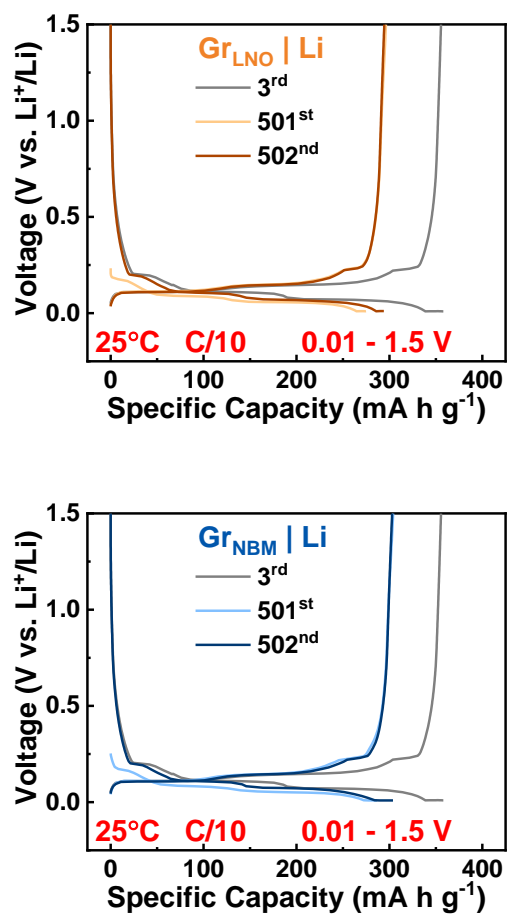
Figure S8. Voltage curves of cycled graphite anodes harvested from LNO and NBM pouch full cells paired with fresh Li-metal anode in half cells.
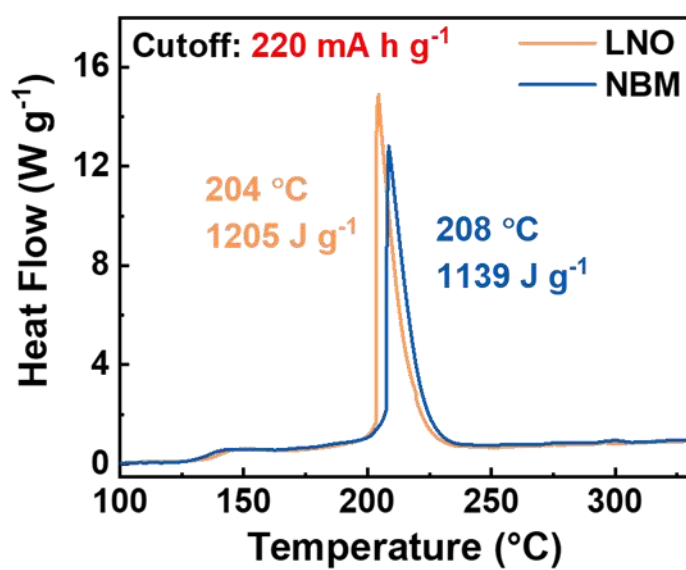
Figure S9. Differential scanning calorimetry profiles of charged LNO and NBM cathodes at 220 mA h g^{-1} (~ 80% state of charge) in half cells paired with Li-metal anodes.
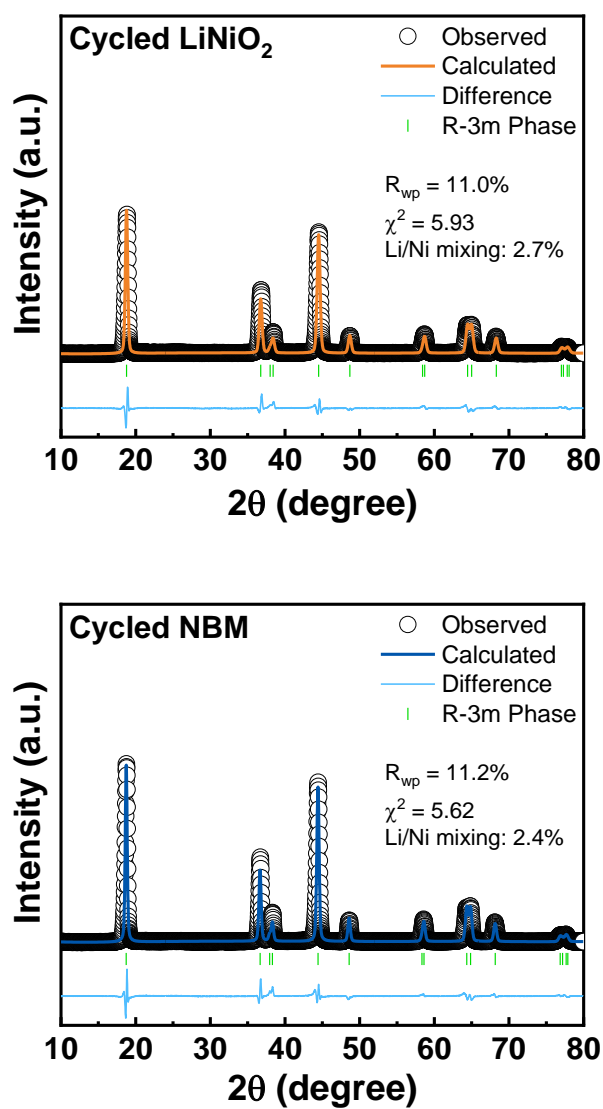
Figure S10. Rietveld refinement results of the LNO and NBM cathode XRD patterns after 500 cycles.
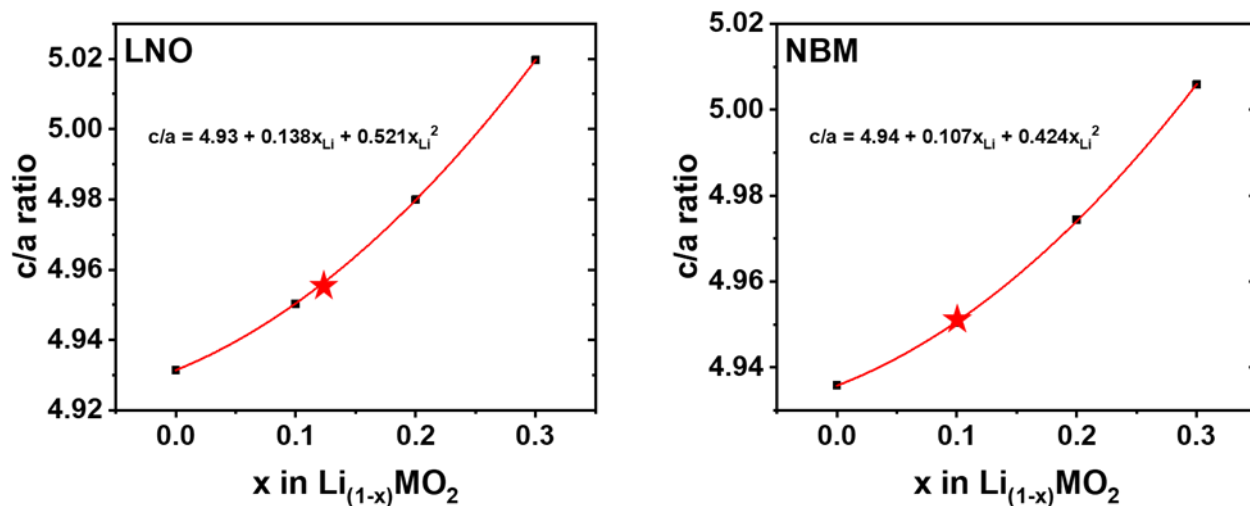
Figure S11. Calibration curves of *c/a* ratio vs. SOC in LNO and NBM electrodes determined from *ex-situ* XRD. The predicted Li deficiencies for the cycled LNO and NBM cathodes are shown with the red star for each curve.

a

	LNO	NBM
BET surface area $(m^2\ g^{-1})$	0.3012 ± 0.0061	0.4360 ± 0.0209

b

BOF^- BOF_2^- $LiBO_2^-$

Figure S12. (a) BET surface areas of the pristine cathode particles. (b) TOF-SIMS 3D rendering visualization of secondary-ion fragments, indicative of complex reaction species with the boron-treated surface and electrolyte species in the cycled NBM cathode after 500 cycles.

Figure S13. SEM images of the cycled graphite anodes that were paired with LNO and NBM cathodes in pouch full cells.

Table S1. Summary of electrochemical performance and cell metrics of other related works

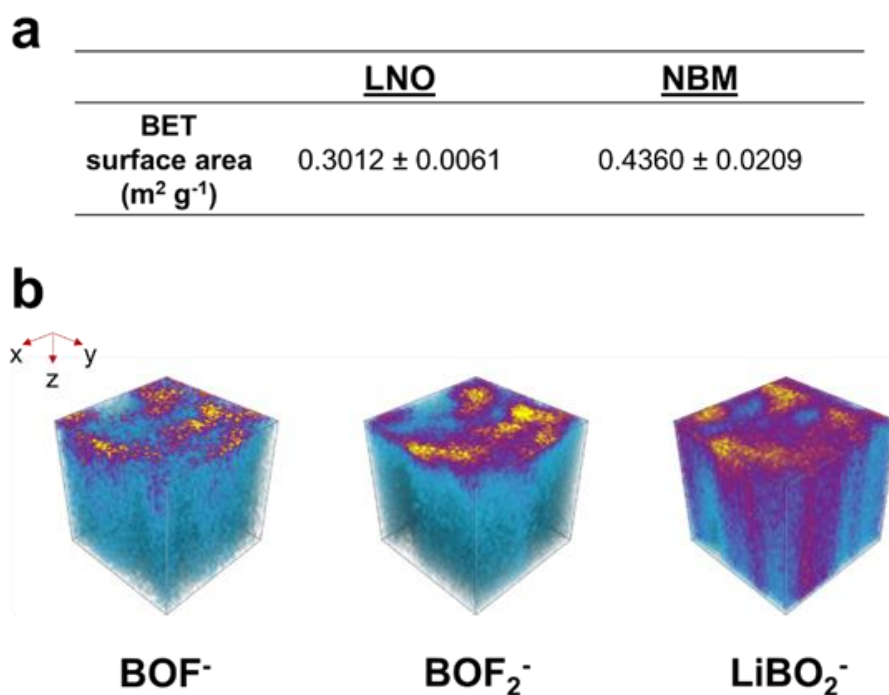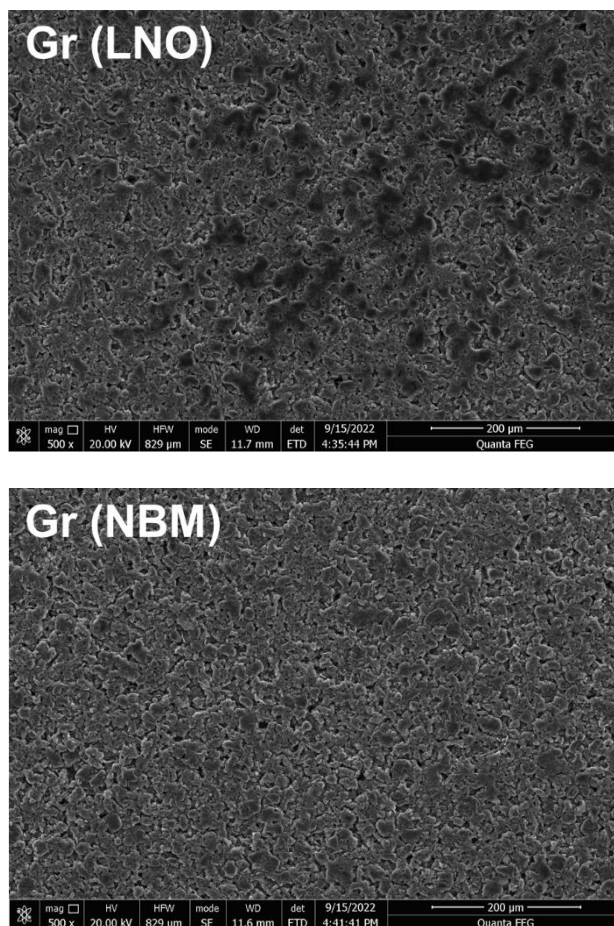| Cathode	Initial capacity (mA h g^{-1}) at given C-rate	Capacity retention, cycle number	Cell type	Areal capacity (mA h cm^{-2})	Voltage range (V)	References
Mg-B LNO	210, 1C	65%, 500	Pouch full cell	2.0	2.5 – 4.2	This work
Li-enriched LNO	~195, C/2	80%, 400	Pouch full cell	~ 1.8 based on C/10 capacity (7.8 mg cm^{-2})	2.8 – 4.2	[1]
W-LNO	~220, C/5	~88%, 100	Coin half cell	Not specified	3.0 – 4.3	[2]
	~165, C/2	79.3%, 100	Coin half cell	~ 1.1 based on C/10 capacity (6 mg cm^{-2})	3.0 – 4.3	[3]
Mg-LNO	216, C/2	78%, 200	Pouch full cell	~ 2.0 based on C/10 capacity (9 mg cm^{-2})	2.5 – 4.3	[4]
Mg-Cu LNO	213, C/2	81%, 200				
Mg-Mn LNO	160, 1C	80%, 200	Coin half cell	~ 1.8 based on C/10 capacity (9 mg cm^{-2})	2.5 – 4.4	[5]
Mg-Ti LNO	200, C/2	82%, 100	Coin full cell	1.4	2.0 – 4.4	[6]
Ti-LNO	235, C/5	~81%, 100	Coin half cell	Not specified	2.8 – 4.3	[7]
Nb-LNO	203.4, C/2	86%, 200	Coin half cell	~ 0.5 based on C/10 capacity (2.5 mg cm^{-2})	3.0 – 4.3	[8]
Cu-LNO	~150, C/2	85%, 100	Coin half cell	Not specified	2.5 – 4.5	[9]
Sb-LNO	117, C/4	88%, 20	Coin half cell	Not specified	2.5 – 4.5	[10]
Al-LNO	157, C/2	81%, 400	Coin half cell	Not specified	2.5 – 4.5	[11]
Mn-LNO	~175, C/2	85%, 200	Coin half cell	Not specified	3.0 – 4.3	[12]

Table S2. Lattice parameters of the pristine and charged cathode XRD patterns in Figure 4e

	LNO		NBM	
	Pristine	**Charged**	**Pristine**	**Charged**
a (Å)	2.877	2.819	2.878	2.816
c (Å)	14.190	13.678	14.206	13.976
V (Å^3)	101.74	94.14	101.90	95.99
Δa		-2.0%		-2.2%
Δc		-3.6%		-1.6%
ΔV		-7.5%		-5.8%

Note that for both charged cathodes, the c lattice parameter was derived from the active H3 phase. For both these results as well as the calibration curves in Figure S11, the c and a lattice parameters as well as the unit cell volumes were calculated using the (003) and (110) peaks, Bragg's law, and geometric knowledge of a hexagonally close-packed (HCP) unit cell with the following equations:

$$c = \frac{3\lambda}{2\sin\theta_{003}} \qquad a = \frac{\lambda}{\sin\theta_{110}} \qquad V = \frac{\sqrt{3}}{2}a^2 c$$

Table S3. Crystallographic parameters of pristine LNO obtained from Rietveld refinement

LiNiO$_2$				Space group: R$\bar{3}$m	
a = 2.8745 Å		c = 14.1898 Å		V = 101.536 Å^3	
R$_{wp}$ = 7.9%				χ^2 = 2.42	
Atom	Wyckoff position	x	y	z	Occupancy
Li	3a	0.00000	0.00000	0.50000	0.9858
Ni (1)	3a	0.00000	0.00000	0.50000	0.0142
Ni (2)	3b	0.00000	0.00000	0.00000	0.9858
O	6c	0.00000	0.00000	0.25850	2.0000

Table S4. Crystallographic parameters of pristine NBM obtained from Rietveld refinement

0.02B-LiNi$_{0.99}$Mg$_{0.01}$O$_2$				Space group: R$\overline{3}$m	
a = 2.8749 Å		c = 14.2058 Å		V = 101.678 Å^3	
R$_{wp}$ = 8.2%				χ^2 = 2.39	
Atom	Wyckoff position	x	y	z	Occupancy
Li	3a	0.00000	0.00000	0.50000	0.9791
Ni (1)	3a	0.00000	0.00000	0.50000	0.0109
Ni (2)	3b	0.00000	0.00000	0.00000	0.9891
Mg	3a	0.00000	0.00000	0.50000	0.0100
O	6c	0.00000	0.00000	0.25827	2.0000

Table S5. Crystallographic parameters of cycled LNO obtained from Rietveld refinement

LiNiO$_2$				Space group: R$\bar{3}$m	
a = 2.8697 Å		c = 14.2184 Å		V = 101.403 Å^3	
R$_{wp}$ = 11.0%				χ^2 = 5.93	
Atom	Wyckoff position	x	y	z	Occupancy
Li	3a	0.00000	0.00000	0.50000	0.9726
Ni (1)	3a	0.00000	0.00000	0.50000	0.0274
Ni (2)	3b	0.00000	0.00000	0.00000	0.9726
O	6c	0.00000	0.00000	0.25597	2.0000

Table S6. Crystallographic parameters of cycled NBM obtained from Rietveld refinement

0.02B-LiNi$_{0.99}$Mg$_{0.01}$O$_2$				Space group: R$\bar{3}$m	
a = 2.8743 Å		c = 14.2306 Å		V = 101.819 Å^3	
R$_{wp}$ = 11.2%				χ^2 = 5.62	
Atom	Wyckoff position	x	y	z	Occupancy
Li	3a	0.00000	0.00000	0.50000	0.9655
Ni (1)	3a	0.00000	0.00000	0.50000	0.0245
Ni (2)	3b	0.00000	0.00000	0.00000	0.9755
Mg	3a	0.00000	0.00000	0.50000	0.0100
O	6c	0.00000	0.00000	0.25538	2.0000

The XRD refinements were carried out with the understanding that B occupies the tetrahedral sites in very small amounts compared to that of the main elements in Li and Ni. Several previous reports address this and additionally discuss the difficulties with implementing such B sites into XRD refinement, which directly correspond to our data as well.[13–18] They address that due to the low proportion of B in the tetrahedral sites as well as the fact that it is a very light element and has low scattering power, it is extremely difficult to affirm the site locations and parameters of the B atom during refinement. As such, the studies comment and show that their refinement parameters do not include B as the much more prevalent Li and Ni atoms will not be greatly affected.[13,18] Regarding our study, this would also apply with the Mg atom, as it is much heavier than B and is easily detected even at 1 mol %. Therefore, given the issues associated with B incorporation, we did not process B into our refinement results in accordance with the previous studies.

Table S7. TOF-SIMS integrated intensity yields for various secondary-ion fragments of interest taken at multiple locations from NBM and LNO cathodes after 500 cycles in full cell configurations

Sample		Secondary ion fragments					
		LiF_2^-	NiF_3^-	PO_2^-	POF_2^-	C_2HO^-	LiO_2^-
NBM	I_{Loc1}	23,500,698	1,050,673	1,582,124	72,272	2,228,836	1,428,071
	I_{Loc2}	13,463,757	493,271	1,981,983	64,201	1,617,811	882,639
	I_{Loc3}	31,099,677	1,769,808	3,528,576	121,784	3,726,336	2,046,655
	I_{Loc4}	14,792,578	543,651	462,367	49,948	1,994,581	1,307,258
	Mean	**20,714,178**	**964,351**	**1,888,763**	**77,051**	**2,391,891**	**1,416,156**
LNO	I_{Loc1}	12,627,306	828,530	1,089,189	19,112	741,359	943,756
	I_{Loc2}	33,979,264	1,299,488	1,364,086	40,879	2,019,425	1,997,865
	Mean	**23,303,285**	**1,064,009**	**1,226,638**	**29,996**	**1,380,392**	**1,470,811**

Table S8. TOF-SIMS integrated intensity yields for various secondary-ion fragments of interest taken at multiple locations from graphite anodes paired with NBM and LNO cathodes after 500 cycles in full cell configurations

Sample		Secondary ion fragments					
		C_2O^-	C_2HO^-	Li^-	LiF_2^-	Ni^-	PO_2^-
Gr_{NBM}	I_{Loc1}	5,390,550	261,190	266,107,443	267,258	93,697	328,311
	I_{Loc2}	4,341,898	197,059	182,234,726	195,676	62,678	216,723
	Mean	4,866,224	229,125	224,171,085	231,467	78,188	272,517
Gr_{LNO}	I_{Loc1}	9,679,504	609,757	107,999,411	307,491	79,150	265,659
	I_{Loc2}	14,924,501	296,064	90,642,893	381,339	450,751	491,870
	I_{Loc3}	17,028,138	265,646	129,484,800	448,287	290,171	380,380
	Mean	13,877,381	390,489	109,375,701	379,039	273,357	379,303

References

[1] T. Zhou, H. Wang, Y. Wang, P. Jiao, Z. Hao, K. Zhang, J. Xu, J.-B. Liu, Y.-S. He, Y.-X. Zhang, L. Chen, L. Li, W. Zhang, Z.-F. Ma, J. Chen, *Chem* **2022**, *8*, 2578.

[2] C. Geng, D. Rathore, D. Heino, N. Zhang, I. Hamam, N. Zaker, G. A. Botton, R. Omessi, N. Phattharasupakun, T. Bond, C. Yang, J. R. Dahn, *Adv. Energy. Mater.* **2021**, 2103067.

[3] D. Goonetilleke, A. Mazilkin, D. Weber, Y. Ma, F. Fauth, J. Janek, T. Brezesinski, M. Bianchini, *J. Mater. Chem. A* **2022**, *10*, 7841.

[4] W. M. Seong, A. Manthiram, *ACS Appl. Mater. Inter.* **2020**, *12*, 43653.

[5] L. Mu, W. H. Kan, C. Kuai, Z. Yang, L. Li, C.-J. Sun, S. Sainio, M. Avdeev, D. Nordlund, F. Lin, *ACS Appl. Mater. Inter.* **2020**, *12*, 12874.

[6] L. Mu, R. Zhang, W. H. Kan, Y. Zhang, L. Li, C. Kuai, B. Zydlewski, M. M. Rahman, C.-J. Sun, S. Sainio, M. Avdeev, D. Nordlund, H. L. Xin, F. Lin, *Chem. Mater.* **2019**, *31*, 9769.

[7] J. Kim, K. Amine, *Electrochem. Commun.* **2001**, *3*, 52.

[8] Q. Hao, F. Du, T. Xu, Q. Zhou, H. Cao, Z. Fan, C. Mei, J. Zheng, *J. Electroanal. Chem.* **2022**, *907*, 116034.

[9] X.-Z. Kong, D.-L. Li, K. Lahtinen, T. Kallio, X.-Q. Ren, *J. Electrochem. Soc.* **2020**, *167*, 140545.

[10] P. Cui, Z. Jia, L. Li, T. He, *J. Phys. Chem. Solids* **2011**, *72*, 899.

[11] X. Kong, D. Li, E. O. Fedorovskaya, T. Kallio, X. Ren, *Int. J. Energy Res.* **2021**, *45*, 10489.

[12] T. Xu, F. Du, L. Wu, Z. Fan, L. Shen, J. Zheng, *Electrochim. Acta* **2022**, *417*, 140345.

[13] Y.-J. Guo, P.-F. Wang, Y.-B. Niu, X.-D. Zhang, Q. Li, X. Yu, M. Fan, W.-P. Chen, Y. Yu, X. Liu, Q. Meng, S. Xin, Y.-X. Yin, Y.-G. Guo, *Nat. Commun.* **2021**, *12*, 5267.

[14] B. Li, H. Yan, J. Ma, P. Yu, D. Xia, W. Huang, W. Chu, Z. Wu, *Adv. Funct. Mater.* **2014**, *24*, 5112.

[15] Z. Feng, R. Rajagopalan, S. Zhang, D. Sun, Y. Tang, Y. Ren, H. Wang, *Adv. Sci.* **2021**, *8*, 2001809.

[16] T. Chen, X. Li, H. Wang, X. Yan, L. Wang, B. Deng, W. Ge, M. Qu, *J. Power Sources* **2018**, *374*, 1.

[17] L. Pan, Y. Xia, B. Qiu, H. Zhao, H. Guo, K. Jia, Q. Gu, Z. Liu, *J. Power Sources* **2016**, *327*, 273.

[18] Z. Sun, L. Xu, C. Dong, H. Zhang, M. Zhang, Y. Liu, Y. Zhou, Y. Han, Y. Chen, *J. Mater. Chem. A* **2019**, *7*, 3375.